Atmos. Chem. Phys. Discuss., 7, 17769–17824, 2007
www.atmos-chem-phys-discuss.net/7/17769/2007/

Atmospheric Chemistry and Physics Discussions

Representativeness and climatology of carbon monoxide and ozone at the global GAW station Mt. Kenya in equatorial Africa

S. Henne[1], J. Klausen[1], W. Junkermann[2], J. M. Kariuki[3], J. O. Aseyo[3], and B. Buchmann[1]

[1]Empa, Swiss Federal Laboratories for Materials Testing and Research, Dübendorf, Switzerland
[2]Forschungszentrum Karlsruhe, Institut für Meteorologie und Klimaforschung IFU, Garmisch-Partenkirchen, Germany
[3]Kenyan Meteorological Department, Nairobi, Kenya

Received: 12 October 2007 – Accepted: 25 November 2007 – Published: 10 December 2007

Correspondence to: S. Henne (stephan.henne@empa.ch)

Abstract

The tropics strongly influence the global atmospheric chemistry budget. However, continuous in-situ observations of trace gases are rare especially in equatorial Africa. The WMO Global Atmosphere Watch programme aimed to close this gap with the installation of the Mt. Kenya baseline station. Here, the first continuous measurements of carbon monoxide (CO) and ozone O_3 at this site are presented. The representativeness of the site was investigated by means of statistical data analysis, air mass trajectory clustering, interpretation of biomass burning variability and evaluation of O_3-CO relationships. Despite its location in equatorial Africa the site was rarely directly influenced by biomass burning emissions, making it suitable for background observations. Located at 3678 m above sea level the night-time (21:00–04:00 UTC) measurements were in general representative of the free troposphere, while day-time measurements were influenced by atmospheric boundary layer air. Six representative flow regimes towards Mt. Kenya were determined: eastern Africa (21% of the time), Arabian Peninsula and Pakistan (16%), northern Africa free tropospheric (6%), northern Indian Ocean and India (17%), south-eastern Africa (18%) and southern India Ocean (21%). The seasonal alternation of these flow regimes was determined by the monsoon circulation and caused a distinct semi-annual cycle of CO with maxima during February and August and with minima in April and less pronounced in November. O_3 showed a weaker annual cycle with a minimum in November and a broad summer maximum. Inter-annual variations were explained with variations in southern African biomass burning and in transport patterns. The measurements at MKN were representative of air masses with little photochemical activity as indicated by weak O_3-CO correlations, underlining the baseline character of the site. Future extensions of the measurement programme will provide better understanding of the atmospheric chemistry of this globally important region.

ACPD

7, 17769–17824, 2007

1 Introduction

Carbon monoxide (CO) and ozone (O_3) are two key species in the photochemical system of the troposphere. Carbon monoxide controls the concentrations and distributions of atmospheric oxidants, such as O_3, hydroperoxy (HO_2) and hydroxyl (OH) radicals. About 70% of OH radicals in the background atmosphere react with CO (Crutzen and Andreae, 1990). Therefore, the concentration of CO largely determines the availability of OH radicals. The OH radical is the main "cleansing agent" of the atmosphere, removing air pollutants or greenhouse gases, the most prominent being methane (CH_4), from the atmosphere. An increase in CO is expected to decrease OH and hence to increase the lifetime and abundance of these gases. CO itself has a lifetime of weeks to months and therefore is a useful tracer for combustion of biomass and fossil fuels (e.g. Fishman and Seiler, 1983; Parrish et al., 1993). CO is emitted from fossil fuel and biomass burning at low temperature and low oxygen conditions. Up to 45% of the total atmospheric CO source results from oxidation of methane and other organics in the atmosphere (Scholes et al., 2003). Global emissions of CO from biomass burning were estimated by Andreae and Merlet (2001) to about 690 Tg CO yr^{-1}, while earlier numbers were given with large uncertainties (280–1190 Tg CO yr^{-1}) (Crutzen and Andreae, 1990). This accounts for almost half of the global annual primary CO emissions (IPCC, 2001; Crutzen and Andreae, 1990). Tropical forest and savanna fires comprise about 50% of these emissions (Andreae and Merlet, 2001) and can therefore significantly lower the oxidative capacity of the troposphere and increase lifetimes of other, climate relevant, gases (Crutzen and Andreae, 1990).

Tropospheric O_3 acts both to control the oxidizing capacity of the atmosphere, by photolysis followed by reaction with water vapor (H_2O) forming OH radicals, and as a greenhouse gas (Levy, 1971; Chameides and Walker, 1973). Ozone is produced in the troposphere by the photochemical oxidation of hydrocarbons, CH_4, and CO in the presence of nitrogen oxides (NO_x=NO + NO_2) (Chameides and Walker, 1973; Crutzen, 1974; Fishman et al., 1979) and is transported downwards from the stratosphere

ACPD
7, 17769–17824, 2007

(Lelieveld and Dentener, 2000, and references therein). Most of the oxidation of long-lived, reduced gases by OH takes place in the tropics, where high UV and humidity promote the formation of OH from the photolysis of O_3 (Logan et al., 1981; Thompson, 1992), which on the one hand represents an important O_3 sink especially over the remote tropical oceans. On the other hand, emissions of O_3 precursors in the tropics have a large O_3 production potential because deep convection can quickly transport surface emissions to the middle and upper troposphere where their lifetimes are increased due to dilution with unpolluted background air and lack of surface deposition (e.g. Pickering et al., 1995). In addition, lightning-produced nitrogen oxides (NO_x) will increase O_3 production. This mechanism has been called "mix then cook" by Chatfield and Delany (1990). Since surface emission of NO_x in tropical countries (especially India and Southeast Asia) are small due to the dominance of biofuel usage and the associated low temperature combustion, O_3 production is often limited (Lelieveld et al., 2001). By means of global chemistry modeling, the contribution of biomass burning to the tropospheric O_3 burden was estimated to 10–15% in the tropics and <10% in the extra-tropics (Lelieveld and Dentener, 2000). The contribution of African biomass burning emissions to O_3 mixing ratios reaches ~24% in the African boundary layer (Marufu et al., 2000) and ~14% for the tropospheric column over Africa (Lelieveld and Dentener, 2000), while the contribution to global tropospheric O_3 was estimated to be 3.2% (Marufu et al., 2000) and 2.4% (Aghedo et al., 2007). Seventy percent of the O_3 produced from African emissions is found off the continent with the largest influence on South America (Aghedo et al., 2007).

Despite these large-scale impacts, atmospheric chemistry over equatorial Africa remains poorly documented. A number of field campaigns were conducted in tropical and southern Africa, mostly focusing on emissions from biomass burning (e.g. SAFARI 1992 Lindesay et al., 1996; TRACE-A 1992 Fishman et al., 1996; SAFARI 2000 Swap et al., 2003). Furthermore, the INDOEX experiment focused on pollution outflow from India over the Indian Ocean and towards eastern Africa during winter monsoon conditions (Lelieveld et al., 2001) and more recently the AMMA research project is

investigating the West African monsoon and its influences on the physical, chemical and biological environment (Redelsperger et al., 2006). In addition to these campaign-based measurements, longer term observations of the O_3 profile over Africa are currently being made within the SHADOZ programme (Thompson et al., 2004) and within the MOZAIC programme (Marenco et al., 1998) onboard commercial aircraft starting from and landing at several tropical African airports (Sauvage et al., 2005). Nevertheless, Thompson et al. (2004) argue that weekly observations of O_3 may not be robust enough for trend analysis in the Tropics due to the strong variability caused by deep convection. For CO, weekly flask sampling data from the tropical African region are available from the Seychelles, Ascension Island and Mt. Kenya through the NOAA ESRL programme (Novelli et al., 2003). Finally, satellite observations of both O_3 and CO are available (e.g. Watson et al., 1990; Edwards et al., 2006b). However, so far these don't provide an adequate vertical profile and might be subject to large uncertainties (e.g. Martin et al., 2002; Newchurch et al., 2001).

Up to now, no long term continuous observations of the composition of the tropical atmosphere over Africa are available. Here we present the first continuous observations of CO and O_3 in tropical Africa as measured at the high altitude Global Atmosphere Watch (GAW) station Mt. Kenya (MKN) in eastern Africa. We focus on the question of representativeness of the station in terms of vertical atmospheric layer and horizontal regions of influence, to discuss the stations' adequacy to serve as a baseline site for tropical Africa. We describe the chemical climatology of the site depending on air mass origin and discuss inter-annual variability in connection with the southern African biomass burning season. O_3-CO relationships are investigated to derive further insight into the photochemical state of the free troposphere (FT) over Kenya. Measurement results are compared to other existing measurements for this region and satellite-retrieved CO concentrations. In the future, these long term continuous observations are expected to be used for trend analysis, satellite and model evaluation and climatological validation of event type data.

2 Methods

2.1 Measurement site

The MKN Global Atmosphere Watch (GAW) (World Meteorological Organization, 2007) station (37.297° E, 0.062° S, 3678 m a.s.l.; 660 hPa pressure equivalent and ~1700 m above the foot of the mountain) is situated on the north-western slope of Mt. Kenya and is surrounded by alpine grassland and bush. As part of the Mt. Kenya National Park the whole mountain area is protected and there are no local anthropogenic emissions, making the site suitable for continuous observations of the background free tropospheric composition. The station consists of two containers with a flat walk-on roof, where the air inlet and meteorological instrumentation is mounted. The containers are presently not air conditioned and undergo temperature variations from ~10°C in the morning to ~20°C in the afternoon. A detailed description of the measurement site, its meteorological instrumentation and the local meteorology can be found in Henne et al. (2007)[1].

2.2 Instrumentation and data quality control

A rain and snow protected air inlet system is mounted 4.5 m above ground and is connected to a glass manifold (length 3 m, diameter 5 cm) to which individual instruments are connected. The manifold is permanently flushed by a high volume pump. Residence times were estimated to be below 10 s.

CO was measured using commercial non-dispersive infrared absorbance (NDIR), gas filter correlation technique (Thermo Electron Corporation TEI 48C TL). Sample air was taken from the glass manifold through a 1.5 m, 4 mm diameter teflon tubing at a flow rate of 1 lpm. A 47 mm teflon filter (5–6 micron) was installed before the sample

[1] Henne, S., Junkermann, W., Klausen, J., Kariuki, J. M., and Aseyo, J.: The Establishment of the Mt. Kenya GAW Station: Installation and Meteorological Characterization, J. Appl. Meteorol. Clim., submitted, 2007.

gas inlet and was regularly exchanged. To reduce the interference from water vapor, a Nafion dryer (PERMAPURE PD-50-24") was installed in the sampling line, operating in reverse flux mode using a critical orifice. A similar setup was described by Nédélec et al. (2003). Due to the container temperature changes the NDIR showed strong zero drift. Therefore, zero air measurements were performed every two h for 20 min. Zero air was generated using a custom built system consisting of a rubin gel cartridge, a SOFNOCAT 423 (Molecular Products Ltd) cartridge, inlet and outlet filters, with a CO scrubbing efficiency of 99.9% for CO levels up to 1%. Since 2004, span gas checks have been performed every two hours for 10 min. A higher concentration laboratory standard (traced back to WMO-2000 CO scale by GAW World Calibration Center (WCC), Empa) was diluted with zero air (using Bronckhorst mass flow controllers) and fed into the span gas inlet. In addition, manual span gas checks directly using 1 ppm laboratory standards (WMO-2000) were performed by the station operators once per month.

All measurements were subject to plausibility checks using time series plots and a semi-automated software tool for data flagging and data storage in a SQL database. Due to drift, CO zero conditions during ambient air sampling were estimated from zero air measurements using local regression models (e.g. Loader, 1999). A span correction was applied in a similar way. The combined uncertainty of every individual 1-min CO measurement was then determined from the contributions of the uncertainty of the CO analyzer, the uncertainty of the zero correction and the uncertainty of the span correction. Data was aggregated to 1-h intervals. The enlarged uncertainty of the 1-h data due to missing values was considered following ISO11222 (ISO, 2002). The average combined expanded uncertainty of the hourly CO measurements was 16 ppb (95% confidence level). We compared our CO measurements with canister samples that were taken weekly (during station visits) for NOAA ESRL (former CMDL) (Novelli et al., 1998b,a, 2003). The relationship between continuous measurements and canister samples was $[CO]_{cont} = 0.96(\pm 0.11)[CO]_{canister}\text{-}2.1(\pm 11.3)$, r=0.79, n=27. The comparison suggests no significant deviation between both mea-

surements. However, there was large unexpected scatter in the individual pairs.

O_3 was measured using commercial UV absorption (254 nm) technique (Thermo Electron Corporation TEI 49, SN: 51959-290). Sample air was taken from the glass manifold through a 1.5 m, 4 mm diameter teflon tubing at a flow rate of 2 lpm. A 47 mm teflon filter (5–6 micron) was installed before the sample gas inlet and was regularly exchanged. The uncertainty of the O_3 measurements was assessed following the analysis of Klausen et al. (2003), taking audit inter-comparisons with Standard Reference Photometer into account. Aggregates and their uncertainties were derived similar to CO. The average combined expanded uncertainty of the hourly O_3 measurements was 3 ppb (95% confidence level).

For both instruments standard operation procedures (SOP) were developed and were followed closely by the station operators. The station was audited by GAW WCC for O_3 and CO in February 2002, February 2005 and February 2006, and measurements were traced back to the GAW Reference Standard (Zellweger et al., 2002, 2005; Klausen et al., 2006). The data discussed here cover the period from June 2002 to June 2006. Due mostly to frequent failures of the power supply at MKN, the data coverage for the 4 year period was only 52 and 49% for CO and O_3, respectively. All time stamps of the hourly data refer to the end of the sampling period. Four-hourly aggregates were derived for use with air mass back trajectories, in a way that the arrival time of the trajectory fell in the center of the 4-h aggregation period.

2.3 Trajectory calculation

Kinematic backward air mass trajectories were calculated on 6-hourly ECMWF analysis fields (T511L60 before February 2006 and T799L91 afterwards) interlaced with 3-hourly forecast fields with $1 \times 1^{\circ}$ horizontal resolution using the trajectory model FLEXTRA (Stohl et al., 1995; Stohl and Seibert, 1998). Trajectories were initialized every 4 h (02:00, 06:00, 10:00, 14:00, 18:00, 22:00 UTC) at station altitude, which corresponds to 1829 m above model ground, and were followed 10 days backward in time. Since Mt. Kenya is an isolated mountain rising high above its surroundings and the following

analysis focuses on long range transport influences, we are confident that the regional scale, horizontal wind speed at the station is best represented by the chosen arrival altitude. The trajectory position was stored every 3 h. Individual air mass trajectories might be subject to calculation errors that arise from uncertainties of the utilized wind analysis or forecast fields, truncation errors due to finite-difference integration scheme or temporal and spatial interpolation errors (Stohl, 1998). Furthermore, subgrid scale processes like convection and turbulent diffusion are not represented by individual trajectories. To cover part of this uncertainty, in addition to the central reference trajectory, 6 uncertainty trajectories were initialized equidistantly spaced on a circle of 0.5° radius around the site at the same altitude above model ground.

2.4 Trajectory clustering

Several different approaches on air mass trajectory clustering to categorize air mass influence on chemical composition measurements are described in the scientific literature (e.g. Moody and Galloway, 1988; Harris and Kahl, 1990; Dorling et al., 1992a,b). Following the approach of Dorling et al. (1992a) we used a combined clustering method that in a first step applied Ward's hierarchical clustering method (Ward, 1963) to determine the number of clusters to retain and in a second step used k-medoids clustering (e.g. Kaufman and Rousseeuw, 1990) to assure the compactness of the derived clusters. With hierarchical clustering the number of clusters to be retained can be determined semi-objectively during the amalgamation process. The relative increase in total within-cluster sum of squared distances for each reduction of the number of clusters will be large when two relatively different clusters are joined. Therefore, the number of clusters should be kept large enough so that no large relative increase occurs. A threshold value of 5% was chosen in this study similar to Dorling et al. (1992a,b); Brankov et al. (1998).

All 3-hourly trajectory positions were used (i.e. a total of 80 points per trajectory) as clustering variables. The sensitivity of the clustering procedure to the choice of the distance measure between trajectory pairs was tested by applying different dis-

tance measures (2-D-Euclidean, normalized 2-D and 3-D-Euclidean, 2-D-spherical, 2-D-spherical plus scaled vertical distance). All distance measures yielded similar results, however we preferred the two-dimensional spherical distance measure to avoid erroneous behavior when trajectory pairs would lie on either side of the date line. No additional weighting was applied to these variables, therefore strong relative differences in trajectory location close to the arrival will cause less absolute distance between two trajectories than differences at their origin. This clustering method thus focuses on differences in the air mass origin and not on differences in the local approach to the site. The clustering was applied to reference and uncertainty trajectories when night-time (22:00 and 02:00 UTC, see Sect. 3.2) CO and O_3 measurements were available. A total of 1592 trajectories were taken into account in the final clustering.

All clustering calculations were performed with the statistics software package R version 2.2.1 (R Development Core Team, 2005). Functions for hierarchical and k-means clustering can be found in the stats package, while k-medoids clustering is available in the cluster package, which implements the algorithms described in Kaufman and Rousseeuw (1990).

2.5 O_3-CO correlations

The O_3-CO relationship has been used to estimate the total ozone production potential of certain O_3 precursor source regions (Fishman and Seiler, 1983; Parrish et al., 1993). It can further serve as a sensitive validation parameter for comparing photochemical models with atmospheric measurements. Both CO and O_3 measurements are subject to uncertainty. Therefore, we used a regression model that takes these uncertainties in both variables into account (Press et al., 1992) weighting the data with the inverse of the measurement uncertainty. Parrish et al. (1998) noted that using a method including measurement uncertainties in both variables instead of the simple approach yielded steeper regression slopes for the O_3-CO relationship. We confirmed this tendency by comparing the Press et al. (1992) approach with reduced major axis regression. However, differences were small for cases with large correlation coefficients.

3 Results and discussion

3.1 Pollution events

As described above, the local environment of the MKN site is mostly free of anthropogenic emissions. However, infrequent, small wildfires might occur within the forest and bush belt of the mountain. These fires emit CO close to the measurement site and therefore can be detected as large peaks in the measured data that disturb the atmospheric background measurements. In order to remove such events from the climatological analysis the measurements were filtered by applying an iterative moving standard deviation filter to CO. Using a window width of 14 days, moving average and standard deviation of CO were computed. Data points outside of three standard deviations of the mean were then removed and the procedure repeated until no new outliers were detected.

If more than two outliers (more than 2 h) were detected on an individual day this day was flagged as a pollution event. Nine different pollution events were detected with this method distributed over 16 of a total of 780 days (2%; see also supplementary material, http://www.atmos-chem-phys-discuss.net/7/17769/2007/acpd-7-17769-2007-supplement.pdf).

The origin of two major events could be traced back to local fire observations made by the station operators, one event could be identified as transport of an aged biomass burning plume (see Sect. 3.6), while the causes of the minor events, with a length of 1–2 days, could not be identified and are thought to be of local origin. All detected events were excluded from the following climatological analysis of the data.

3.2 Diurnal cycle

Not only local sources and sinks but also the influence of variable atmospheric boundary layer (ABL) depth might cause strong diurnal variations of atmospheric trace gases. Especially at high altitude sites the question arises which vertical atmospheric layer

the measurements are representative of. Henne et al. (2007)[1] observed a frequent development of slope wind circulations at MKN and turbulent vertical transport of boundary layer air towards MKN during day-time. These transport processes manifest themselves in a pronounced diurnal cycle of CO mixing ratios (Fig. 1). Shortly after sunrise (04:00 UTC) CO starts to rise as a result of advection of more polluted ABL air and reaches a maximum between 11:00 and 13:00 UTC. The average diurnal amplitude was 15 ppb. This pattern recurs during all months of the the year, with an increased amplitude (25–30 ppb) during July and September.

For O_3 the diurnal cycle is inverse to that of CO with a day-time minimum and night-time maximum with an average amplitude of 4 ppb. The amplitude of the O_3 diurnal cycle was larger in the months of December and January. The day-time minimum of O_3 is thought to have two different causes. On the one hand, due to surface dry deposition, O_3 mixing ratios in the ABL over Kenya are usually smaller than those in the FT (Thompson et al., 2004), see also Sect. 3.7.2. Advection of ABL air would therefore decrease O_3 mixing ratios at MKN. On the other hand, O_3 might also be photochemically destroyed in the FT under low nitrogen oxides (NO_x) conditions likely for the clean East African area (Klonecki and Levy, 1997).

The diurnal cycle was expected to be different for days with and without influence from the ABL. In order to distinguish between these two categories we used the criterion described by Henne et al. (2007)[1] categorizing days by the diurnal course of wind speed and direction and specific humidity. In a first step, this two-step criterion distinguished between days that showed a thermally-driven flow system (therm) and days that were synoptically driven (syn). In a second step, days that showed a significant increase in specific humidity (var) – used as a tracer for boundary layer air – were separated from days with insignificant variation in specific humidity (const). CO measurements at MKN showed different diurnal behavior for the different categories (Fig. 2). CO experienced the strongest diurnal cycle with mixing ratios peaking in the afternoon hours on days that showed a significant increase of specific humidity (category var), with an average CO amplitude of about 20 ppb. The cycle was more pronounced for

the thermally-influenced days (therm) than for the synoptically-influenced days (syn). On days that did not show a significant increase in specific humidity (const), the CO cycle was less pronounced and larger night time concentrations of CO (+5 ppb) were observed, indicating the presence of residual layers in the FT. However, these conditions only occurred during less than 25% of all nights and might have other causes than residual layers. Therefore, these data were retained for the climatological analysis. In general, the day-time measurements of CO at MKN reflect a mixture of free tropospheric and boundary layer air.

The O_3 diurnal cycle was amplified during days that showed significant increase in specific humidity (var), when lower afternoon and higher night-time values were observed. Conversely, during days that did not show a significant increase in specific humidity, the afternoon O_3 minima were less pronounced. The diurnal cycle of ozone concentrations for the different categories compares well with the findings of the CO diurnal cycle in that days with stronger ABL influence experience lower O_3 and higher CO afternoon concentrations.

In summary, throughout the whole year measurements at MKN were representative of free tropospheric conditions during night-time (21:00–04:00 UTC) only, while during day-time a mixture of boundary layer and free tropospheric air was usually sampled. All further climatological analysis of the MKN measurements was therefore restricted to the free tropospheric observations (21:00–04:00 UTC).

3.3 Annual cycle and large scale advection

The overall average free tropospheric hourly CO mixing ratio at MKN was 94±16 ppb ($\hat{\mu}\pm 2U$, k=2, night-time data only). CO experienced a pronounced annual cycle (Fig. 3a and Table 1). The largest mixing ratios were recorded for the months January to March, followed by a sharp decrease towards April and May and a recovery by the end of the year. In 2003 a strong increase in CO mixing ratios in the months of July and August led to a secondary maximum in the annual cycle and also induced a secondary maximum in the overall annual cycle. All other years showed average

CO concentrations during this time of the year. The overall average free tropospheric hourly O_3 mixing ratio at MKN was 29±3 ppb ($\hat{\mu}\pm 2U$, k=2, night-time data only). In contrast to CO, O_3 mixing ratios showed little deviation from the overall mean from January to May (Fig. 3b and Table 1). For the months June to September, O_3 as well as CO mixing ratios were enhanced, while for the months October to December, O_3 mixing ratios were reduced by about 5 ppb.

The general annual cycle of CO and O_3 at MKN can be explained by the seasonal variation of monsoon flow over equatorial East Africa (Fig. 4), which is dominated by the seasonal displacement of the inter-tropical convergence zone (ITCZ) (Asnani, 1993; Leroux, 2001; Slingo et al., 2005). Throughout boreal winter, the ITCZ is situated south of the equator (10–15° S) extending from the northern tip of Madagascar towards southern Tanzania and then northward towards Lake Victoria. Consequently, East Africa is generally dominated by north-easterly monsoon carrying northern-hemispheric air towards Kenya that is enriched in CO during the winter season (Novelli et al., 1998a, 2003). When the ITCZ starts to progress northward again, it brings a period of "long rains" from mid-March to the beginning of June to equatorial East Africa and with it clean air from the Indian ocean, causing the distinct spring-time minimum in CO. During boreal summer, the ITCZ is situated far to the North over India (15–20° N) and along the southern coast of the Arabian Peninsula (10–15° N), resulting in southerly to south-easterly winds over Kenya. CO mixing ratios in the southern hemisphere increase during boreal summer due to enhanced biomass burning emissions (Novelli et al., 1998a, 2003) and peak in boreal fall (Bremer et al., 2004; Edwards et al., 2006a). Consequently, increased CO and O_3 concentrations are transported towards equatorial Africa from June to October. When the ITCZ crosses over Kenya from mid-October to December it brings a second rainy period with strongly reduced O_3 but only slightly reduced CO concentrations. This might indicate flow from the northern hemispheric marine boundary layer where O_3 is photochemically destroyed at rates of 2–6 ppb d^{-1}, while CO concentrations are increased due to pollution outflow from India (Lelieveld et al., 2001). From a meridional cross section of O_3 soundings in the Indian

Ocean in February/March 1999 Saraf et al. (2003) report the lowest O_3 mixing ratios within the maritime boundary layer in the ITCZ. Mixing ratios were below 30 ppb up to 650 hPa, which is in line with the MKN O_3 measurements during ITCZ passage around November.

3.4 Regions of influence

Depending on the flow regime, an individual site might be representative for various, discrete areas. Six different regions of influence were determined for MKN by trajectory clustering. These air masses are presented in Fig. 5 in the form of residence time plots for individual trajectory clusters and can be described as follows:

East Africa (EA, Fig. 5a): this cluster describes situations with relatively low wind speeds, air originating relatively close to the surface and possible recirculation over eastern Africa. It represents 21% of airflow towards MKN. Advection was mostly from the East with little contribution from the West, though with generally lower wind speeds.

Arabian Peninsula (AP, Fig. 5b): during 16% of the time advection towards MKN was from the Arabian Peninsula and Pakistan across the Horn of Africa. The transport was in general directed downward within the Arabian high pressure system.

Northern Africa (NA, Fig. 5c): air masses combined in this cluster contributed 6 % and were transported downward from the upper troposphere with little contact with the surface and originated over western North Africa. Part of the flow occurred close to or within the subtropical jet as indicated by large wind speeds.

Southern Indian Ocean (SIO, Fig. 5d): advection was mainly over the south-western Indian Ocean with most air masses arriving over Africa at the coastline between Kenya and Tanzania. The northern end of Madagascar was often within the catchment area of this air stream. The flow was close to the surface and in general ascending towards the East African highlands and can be associated with flow within the active phase of the East African Low Level jet (Findlater, 1969). It contributed 21% to the total flow towards MKN.

Southern Africa (SA, Fig. 5e): in contrast to the SIO cluster, air flow was more from

the south along the coastal areas of Tanzania and northern Mozambique and often originating over Madagascar. In total SA contributed 18% to air flow towards MKN. Air masses stayed close to the ground during most of the transport and were in contact with the surface over Malawi and eastern South Africa.

Northern Indian Ocean (NIO, Fig. 5f): during 17% of the time advection was from India over the northern Indian Ocean. Often the air masses stayed at altitudes higher than 2000 m a.g.l. and therefore above the trade wind inversion.

The distinct seasonal pattern of the monsoon flow over the Indian Ocean can be seen in the varying occurrence of the individual clusters during the year (Fig. 6 and supplementary material). The situations with northern hemispheric advection dominated from November to March, while the southern hemispheric situations dominated from May to October. The EA cluster could be observed all year round with largest contributions during the rainy seasons, i.e. April and October. The descending flow pattern NA was most prominent from January to May. Although the contribution of the AP cluster was smaller during summer it did not cease completely as did the contribution of the NIO and NA clusters. In general, the air mass categorization using trajectory clustering yielded similar results to those reported before for the airflow towards Kenya by Gatebe et al. (1999). They manually categorized backward trajectories for the years 1991 to 1993, resulting in 6 categories that were slightly different from the ones described in this study. Instead of two categories of advection from the northern and southern Indian Ocean respectively (AP, NIO and SA, SIO in our study) they categorized these cases as one for each hemisphere. In contrast, they describe a category of very rare westerly air flow arriving from the Atlantic Ocean after crossing equatorial Africa that was not observed during our study period. Furthermore, they observed two types of recirculation patterns within Kenya and eastern Africa that compare to our EA category. Apart from this, our findings for the annual cycle of different air mass contributions agree well with their study.

Due to variations in CO background mixing ratios and emission source strengths from biomass burning, CO mixing ratios within the different clusters also showed a

strong annual cycle (Fig. 7a and Table 2). The cycle for the EA category was similar to the overall annual cycle, showing a semi-annual pattern with a pronounced minimum during April/May and a less pronounced minimum in November. The boreal spring maximum seen for the AP category was more pronounced than average, while concentrations stayed low during boreal summer. The AP category therefore was clearly dominated by the northern hemispheric CO annual cycle. Although originating from higher altitudes, air masses within the NA category also experienced a boreal springtime maximum and lower concentrations throughout the rest of the year, representing northern hemispheric, free tropospheric conditions. A similar annual cycle was observed for NIO conditions, however, with generally lower CO concentrations when compared to NA conditions. This is surprising since large CO concentrations were expected from the winter-time outflow of emissions from India. This outflow, however, is confined to the marine boundary layer below 4 km and its vertical extent is limited by the trade wind inversion (de Laat et al., 2001). CO mixing ratios from January to March within the NIO category were around 100 ppb, similar to those reported by de Gouw et al. (2001) for the altitude range 3–8 km (100–130 ppb), but considerably lower than the previously reported 140 ppb for the marine boundary layer over the northern Indian Ocean during this season (Stehr et al., 2002). The MKN O_3 mixing ratios during the same period were in the range of 30 ppb and comparable to measurements in the maritime boundary layer that were under northern hemisphere, continental influence (Stehr et al., 2002), but higher than the average maritime O_3 (~ 20 ppb) for the 3–8 km altitude range (de Gouw et al., 2001).

In contrast to the northern hemispheric categories, the southern hemispheric categories showed an annual cycle with pronounced maxima in the boreal summer and lower concentrations during boreal winter. Thus, the SA category exhibited a larger maximum driven by biomass burning emissions from continental Africa, while the SIO category was representative for the southern Indian ocean background with the lowest CO of all between February and June.

Ozone showed less between-category variation than CO (Fig. 7b and Table 2). Most

categories showed a minimum from October to December. There was a tendency to larger O_3 concentrations for the NA category most likely due to the origin at higher altitudes. In contrast, O_3 was lowest in the SIO category due to the origin in the marine boundary layer of the remote Indian Ocean. Both SA and SIO showed an O_3 maximum during boreal summer, the southern hemispheric biomass burning season. The maximum was more pronounced for the continental origin (SA) than for the maritime origin (SIO). However, the maximum was less distinct than that observed by MOZAIC flights within the lower FT (O_3=80–100 ppb) over western equatorial sites in Africa, but agreed with the observation of only small O_3 enhancements during boreal summer over Nairobi (Sauvage et al., 2005). During SAFARI 2000 even larger O_3 (>120 ppb) concentrations were observed over Zambia in a layer reaching from 800 to 500 hPa as a result of pollutant recirculation within the south African haze layer (Thompson et al., 2002).

3.5 Inter-annual variability and southern African biomass burning

Inter-annual variability in the CO and O_3 observations at MKN can be caused by both variability in the transport patterns and variability in CO emission strengths, mainly from biomass burning. Inter-annual variability was largest during the southern hemispheric biomass burning season (Fig. 3). The temporal evolution and inter-annual variability of CO concentrations during this season can be understood by considering the southern African biomass burning season.

During the southern hemispheric biomass burning season, stable high pressure conditions exist over large parts of southern Africa, hindering vertical transport and favoring accumulation and recirculation of biomass burning emissions over the area ("south African haze layer", Garstang et al., 1996). Export of pollution takes place off the coast of Angola by easterly tropical wave disturbances and off the coast of Mozambique and South Africa by westerly mid-latitude wave disturbances. The frequency of westerly disturbances reaches a maximum in October (Garstang et al., 1996). Moreover, the El Niño Southern Oscillation (ENSO) causes changes not only in precipitation amount

ACPD
7, 17769–17824, 2007

over southern Africa (El Niño years are connected with drier conditions throughout boreal summer and spring (e.g. Webster et al., 1999; Goddard and Graham, 1999; Indeje et al., 2000)), but also in the frequency of wave disturbances clearing out the south African haze layer (Singleton and Reason, 2007). During the SAFARI 2000 experiment, a year with La Niña conditions, a typical southern African haze layer was observed during August/September that extended up to 3.5 km in the south of the fires and up to 6 km in the humid savanna region. Typical mixing rations of CO were 200–650 ppb within this layer and <120 ppb above in the FT, while O_3 within the layer ranged from 30 to 100 ppb (Yokelson et al., 2003). Hely et al. (2003) conclude that arid areas produce heavier fuel loads during wet years, while humid areas react in the opposite way. According to Swap et al. (2003) and Edwards et al. (2006a) pollutant concentration within the south African haze layer reach maximal concentrations from August to October, while maximum fire activity, as observed by satellite-detected burnt area, peaks in June/July (Silva et al., 2003). To elucidate this discrepancy we analyzed fire counts as retrieved by Moderate Resolution Imaging Spectroradiometer (MODIS) sensors on board NASA satellites Terra and Aqua (Justice et al., 2002; Giglio et al., 2006) on a regional basis for the years 2002–2006. To account for spatial variability in the frequency of satellite overpasses and missing observations and to reduce the effect of day-to-day variation in fire counts due to clouds, the climate modeling grid fire count product (cloud-and-overpass corrected) was used with a horizonal resolution of 0.5°×0.5° and monthly temporal resolution as described by Giglio et al. (2006). Southern African countries were grouped as follows: (Central) Zambia, Angola, Dem. Rep. Congo; these regions were not directly covered by any of the MKN footprints, but large scale emissions might still increase the continental scale background and therefore influence MKN during SA conditions. (eastern) Mozambique, Zimbabwe, Malawi, Madagascar; (southern) Botswana, South Africa, Swaziland, Namibia. The eastern and southern region lie well within the footprint of the SA pattern and will therefore directly influence measurements at MKN, while the SIO regime only touched the very eastern parts of these regions. Kenya and Tanzania were treated separately to estimate the local to

regional influence of biomass burning on MKN.

The overall fire count maximum was reached in August (Fig. 8a), while for the central region, the largest contributor to total fire counts, the maximum was reached earlier in July/August, slightly later than observed during the La Niña year 2000 (Silva et al., 2003). In the eastern and southern region fire counts peaked in September. Their overall contribution to total fire counts was small, while the contribution of Tanzania and especially Kenya itself was negligible. The shift of peak fires from earlier in the year in the central western parts of southern Africa to later in the year in the southern and eastern parts was also observed for the year 2000 (Silva et al., 2003). The question remains, though, of why fire counts peak before pollutant concentrations. Fire counts are not proportional to pollutant emissions but the latter depend on the amount and type of vegetation burned, and the burning conditions. Fire radiative power (FRP) which is also retrieved from the MODIS instruments, offers a quantity that is more proportional to the amount of biomass burnt (Wooster et al., 2005; Roberts et al., 2005). With respect to the seasonal cycle of the MODIS FRP in southern Africa, the contribution of the central region is less dominant, although the contribution of Tanzania and Kenya still remains small (Fig. 8b). Furthermore, the month of peak FRP (September) was delayed by one month compared to the fire count seasonal cycle, which is in better agreement with the observed maximum pollutant concentrations. In contrast to the sharp decrease in fire counts in October, FRP remained high especially in the eastern region, sustaining high pollutant levels. An additional factor increasing emissions at the end of the biomass burning season might be the transition from the burning of less dense vegetation in the western part of southern Africa earlier during the year to denser vegetation in the eastern part from August to October. This phenomenon might be coupled to a transition from more efficient burning conditions to less efficient conditions, when dense vegetation tends to burn in smoldering fires.

Pollutants emitted in the eastern southern African region from August to October might be readily exported towards the Indian Ocean and then northward towards East Africa. However, CO concentrations at MKN showed a broad boreal summer maximum

ACPD
7, 17769–17824, 2007

with the highest concentrations somewhat earlier than observed in southern Africa and as deduced from FRP. Continental SA transport towards MKN was maximal in July and ceased afterwards, while the SIO pattern dominated from August to October (Fig. 6). Therefore, the peak CO concentrations observed at MKN in July/August can be explained as a combination of increased occurrence of the SA transport pathway and moderately increased CO concentrations over southern Africa, while during September/October, when concentrations maximize in southern Africa, transport towards Kenya tends to be more directly from the Indian Ocean (cluster SIO).

Inter-annual variability in regional fire count occurrence (Fig. 9) and in the two dominating transport patterns in boreal summer (SA and SIO, Fig. 10) were used to explain variations in the MKN observations. The most prominent anomaly in monthly CO concentrations was observed in July/August 2003, when concentrations reached an overall summer-time maximum. This increase was most likely caused by more frequent transport in category SA throughout the whole summer 2003, while, especially for August, the contribution from SIO was lower than in other years. No increase in biomass burning as determined from regional FRP sums was observed. Average biomass burning occurred in the eastern and central region. Local (Kenyan) biomass burning activity was above average from August to October of that year and might have contributed to CO levels in August. Although CO was strongly enhanced during August 2003, O_3 was below average. However, the correlation between O_3 and CO was relatively large (r^2=0.3), indicating the photochemical origin of O_3. The low concentrations might therefore reflect variability in larger scale horizontal or vertical advection.

In June 2005 both CO and O_3 concentrations were above average (Fig. 3). Although Edwards et al. (2006b) observed little inter-annual variation in fire counts for the whole south African subcontinent, we detected strong inter-annual variability on the regional scale. Biomass burning in the eastern region was intensified in 2005 throughout the early burning season, starting as early as March and remaining elevated until the end of July 9. Since transport from SA in June 2005 was reduced 10, the increased CO at MKN was most likely caused by increased emissions in the eastern biomass burning

region. In general, CO concentrations were low in July/August 2002, caused by less frequent transport from southern Africa. Below average CO concentrations in May 2005 occurred together with increased transport of clean air from the southern Indian Ocean. Increased CO concentrations observed in November 2002 (when advection towards MKN was more directly from the east) were associated with increased biomass burning over Indonesia (Edwards et al., 2006b).

3.6 O_3-CO correlations

For each year, monthly O_3-CO correlation coefficients were calculated for the 1-hourly night-time measurements at MKN (including pollution event data that were previously omitted from the climatological study). Significant correlations (R^2>0.2, p<0.01) were only observed for some individual months and not for all years. Only for May and October were O_3-CO correlations significant for 3 out of 4 years with slopes of 0.8 - 1.6 and 0.8 - 2, respectively. The Tropospheric Emission Spectrometer (TES) retrieves O_3 and CO concentrations at 618 hPa. Global maps of O_3-CO correlations were obtained for July 2005 (Zhang et al., 2006). In agreement with our results no significant ($|R|$<0.2) correlations were found over equatorial eastern Africa, while in central to southern Africa slopes were between 0.6 and 0.8. These low correlations can be indicative of very aged air masses or of air masses with different background concentrations influencing the station within the same month (Parrish et al., 1998).

Separating the O_3 and CO measurements by air mass origin, correlations were calculated for different influence regions. Overall only the SIO origin showed a significant correlation when taking all data into account, with a slope of 1.1 and R^2=0.25. On a monthly basis correlations for different air mass origin improved, with the largest correlations (R^2=0.6 – −0.8) for the SIO cluster from April to June and a slope of 0.5–1. This might be indicative of photochemical destruction of both species over the remote Indian Ocean. The correlation was also slightly significant (R^2=0.25) for the SA cluster in September with a slope of 0.4 that is more representative of recent biomass burning plumes.

Although MKN was rarely directly influenced by biomass burning events, these were evaluated in terms of their O_3-CO relationship. To determine events with increased CO related to biomass burning, MODIS fire counts (0.5°×0.5° horizontal and 8 day temporal resolution) were evaluated along the back trajectories arriving at MKN. Fire counts along each back trajectory were summed for the reference and the uncertainty trajectories at times when the trajectory was less than 2000 m above model ground. A weighted average fire count for each arrival time was then derived by giving a weight of 1 to the reference and 1/6 to each of the 6 uncertainty trajectories. Biomass burning events were then defined as times when fire counts were larger than their overall third quantile and CO mixing ratios were at least 16 ppb (expanded uncertainty of 1-hourly data) larger than the background CO concentrations. The CO background was estimated using the Robust Extraction of Background Signal (REBS) method of Ruckstuhl et al. (2007)[2] applying a tuning constant b of 3.5, a 60 day window width and the "residuals below the mode" scaling function. All night-time CO measurements, also at times excluded for the climatological analysis, were used. Of the selected times only continuous periods with at least 12 data points (which is equivalent to 1.5 days due to the use of night-time data only) were kept for regression analysis. Estimated correlation coefficients further had to satisfy R^2>0.2 and p<0.01.

With these criteria only 4 significant biomass burning events remained within the four year period, again underlining the baseline character of the MKN site. The mean age of the plumes was estimated from the time along the back trajectories when the fire counts were "picked-up", using weighted average of the time with fire counts as weights. The slope of the O_3-CO relationship increased with plume age from 0.2±0.02 for a 3.1±0.1 day old plume to 0.62±0.12 for a 4.7±0.3 day old plume (Fig. 11 and Table 3). Of the four detected events three were of northern hemispheric origin with pollutants being released from biomass burning in eastern Sudan and western Ethiopia, as is shown by

[2]Ruckstuhl, A., Henne, S., Reimann, S., and Hglin, C.: Estimation of background concentrations of atmospheric trace gases using robust local regression, Atmos. Chem. Phys. Discuss., in preparation, 2007.

the back trajectories overlayed on the fire count map for the most pronounced plume in February 2004 (Fig. 12). Note that this event was already identified as a pollution event in Sect. 3.1 and was therefore not included in the climatological analysis. The remaining plume was of southern hemispheric origin, carrying biomass burning emissions from Madagascar and northern Mozambique.

Increasing slopes of the O_3-CO relationship with the age of biomass burning plumes have been observed before. Our estimates agree well with estimates taken from flight campaigns near the southern African biomass burning region or over the tropical South Atlantic. As part of the CITE-3 flight campaign $\Delta O_3/\Delta CO$ enhancements in the range 0.2–0.7 were observed for aged (7–10 d) biomass burning plumes (Andreae et al., 1994). During TRACE-A over southern Africa, South America and the South Atlantic, Mauzerall et al. (1998) derived $\Delta O_3/\Delta CO$ of 0.15±0.37 for fresh biomass burning plumes (<0.2 d), 0.32±0.76 for recent plumes (≤1 d), 0.71±0.12 for aged plumes (≤5 d) and 0.74±0.9 for old plumes (>5 d). They suggest a correction of about −20% for older plumes due to loss of CO during transport. During the SAFARI August/September 2000 experiment in southern Africa Yokelson et al. (2003) observed slopes of 0.09 in fresh (<1 h) biomass burning using airborne FTIR measurements. This slope increased to 0.22 for biomass burning haze with age 2-4 days. For the same campaign, detailed information of the evolution of $\Delta O_3/\Delta CO$ in biomass burning plumes observed over Namibia is given by Jost et al. (2003). $\Delta O_3/\Delta CO$ increased from 0.07 at 1 h after the emission to 0.1 after two h. Model simulations successfully reproduced the O_3 measurements. For fresh (<0.5 d) biomass burning plumes in northern Australia during the 1999 BIBLE-B experiment Takegawa et al. (2003) estimated a $\Delta O_3/\Delta CO$ slope of 0.12±0.04. For average vertical profiles of CO as obtained by MOPITT and O_3 from sondes, Bremer et al. (2004) derived a fractional increase of $\Delta O_3/\Delta CO$ of 0.2–0.4 from May to October over Natal, Brazil. During PEM-Tropics-A over the remote South Pacific $\Delta O_3/\Delta CO$ slope was determined to 0.75 in three plumes of aged biomass burning pollutants originating in southern Africa and northern Australia (Singh et al., 2000).

ACPD
7, 17769–17824, 2007

EGU

3.7 Direct inter-comparison with other measurements

To further support our findings on the representativeness of the MKN measurements, these can be compared directly with satellite and other in-situ observations in the covered region of East Africa and the western Indian Ocean.

3.7.1 Horizontal distribution of CO

To derive an areal picture of the CO distribution over eastern Africa and the western Indian Oceans we calculated seasonal trajectory statistics using all night-time CO measurements from MKN between 2002 and 2006. The corresponding trajectories and the technique proposed by Seibert et al. (1994) and Stohl (1996), extended by Reimann et al. (2004), was here applied with the additional constraint that only trajectory points between the surface and 600 hPa were evaluated. Using trajectory statistics, an individual point measurement in time is assigned to a certain area, the source region of the air mass, as represented by back trajectories. Thus, an areal distribution of the measured pollutant is generated by the superposition of a large number of measurements and back trajectories assuming that the large scale distribution of the pollutant or its sources does not change significantly with time. Obviously, this is not fulfilled for biomass burning emissions within the course of a year. Therefore, distributions were derived on a seasonal basis. Due to the distinct advection pattern towards MKN some areas are better represented than others at various times of the year.

Figure 13 shows the horizontal distribution of CO as derived from the trajectory statistics separately for the four seasons. During winter a well defined north-south gradient of CO existed over the Indian Ocean. Furthermore, CO was increased in northern Africa, west of the Ethiopian Highlands, which coincides with the area of northern hemispheric biomass burning. CO also increased towards India. The southern Indian Ocean was not seen by MKN during winter at all. In spring, CO concentrations generally decreased in comparison to winter. CO still remained high on and close to the continent in the north. In contrast, the southern Indian Ocean largely showed

very low CO concentrations. In summer of the northern hemisphere only the Arabian Peninsula was visible for MKN, showing even more decreased CO concentrations. In the southern Indian Ocean, however, CO increased, especially close to the continent and around Madagascar, while the remote southern Indian Ocean remained under low CO concentrations. In fall the area of elevated CO had spread also into the remote southern Indian Ocean. Only a small band around the Equator remained unpolluted.

These results can be compared to seasonal averages (covering the same years as the MKN measurements) of satellite-retrieved CO from Measurement of Pollution in the Troposphere (MOPITT) onboard NASA satellite Terra (Deeter et al., 2003) at 700 hPa. Since the measurement technique relies on the thermal contrast between the surface and atmosphere, the retrieval depends on surface temperature and shows little sensitivity to CO in the boundary layer during night-time (Edwards et al., 2006a). Therefore, we compared only night-time retrievals with the MKN trajectory statistics that are more representative for the FT.

While general features of the seasonal CO distribution agreed quite well between the trajectory statistic (Fig. 13) and the MOPITT measurements (Fig. 14), substantial differences in the absolute concentrations were observed. Over the Indian Ocean, relative differences ranging from −40 to +20% (MOPITT - MKN) occurred, while over land estimates from MOPITT were in general larger than estimates from MKN trajectory statistics (+40%). Differences close to the receptor site MKN were in the range −20 to +20 %. Relative differences were smallest during boreal fall when CO reaches maximum concentrations in the southern hemisphere.

Previous inter-comparisons between MOPITT and in situ profiles showed good agreement, with the bias mean and standard deviation for the retrieved CO column being −0.5±12.1% (Emmons et al., 2004; Deeter et al., 2003). MOPITT 700 hPa monthly means for the lower southern hemisphere (0–30° S) were compared with CO from NOAA ESRL flask sampling network (Edwards et al., 2006b). MOPITT measurements were clearly larger than in-situ measurements most likely due to different sampling altitudes and different geographic representation. In addition to these sources of

discrepancy, our large disagreement between MOPITT and MKN most likely can be attributed to uncertainties connected to the trajectory statistics. In particular, grid cells at the edge of the CO field produced by the trajectory statistic should not be interpreted due to infrequent contributions of these grid cells. CO loss during the transport to MKN might create a negative bias for regions further away from MKN. Taking a lifetime of CO of 20 days for the tropical atmosphere below 6 km a.s.l. into account (Mauzerall et al., 1998), 15 to 19% of CO might have been lost during transport to MKN after 5 to 10 days, respectively.

3.7.2 SHADOZ O_3

Regular O_3 observations to MKN are performed in the context of the SHADOZ programme at Nairobi about 150 km south-west of MKN (Thompson et al., 2004). A total of 212 O_3 soundings were available for the period investigated (June 2002 to June 2006) and for 101 soundings the corresponding O_3 measurements were available from MKN. Soundings were usually started between 07:00 and 10:00 UTC. Since the MKN site might already be influenced by up-slope flow at this time of the day, MKN O_3 measurements of the previous night (21:00–04:00 UTC) were compared with the sounding results within a 500 m thick layer centred around the station altitude. Linear regression yielded $[O_3]_{sounding}=1.29(\pm0.04)[O_3]_{MKN}-0.4(\pm1)$, $R^2=0.57$, $n=101$. Comparison of the means indicated an average absolute difference of $[O_3]_{sounding}-[O_3]_{MKN}$ 7 ppb. This result did not improve when only MKN measurements from 01:00 to 04:00 UTC were used. The large positive difference might be due to uncertainties in the O_3 soundings at low O_3 mixing ratios, different air streams affecting either site at the same time or due to surface deposition of O_3 before reaching the MKN measurement site. The latter could be caused when down-slope flow transports free tropospheric air towards MKN within a shallow surface layer during night-time.

The annual cycle of O_3 measurements at MKN and for different 500 m thick altitude ranges over Nairobi showed a similar pattern with maxima in February/March and June to September (Fig. 15). However, the cycle was less pronounced at MKN,

especially the broad boreal summer maximum as seen in the soundings was not as clearly identified at MKN. In general, the cycle at MKN agreed better with the lower altitudes centered at 2250 (surface layer) and 2750 m a.s.l. than with the layer centered at station altitude (3750 m a.s.l.). The less pronounced O_3 maximum in the surface layer was probably caused by night-time O_3 surface deposition and O_3 titration by fresh NO emissions in the Nairobi metropolitan area. The soundings were done in the morning hours before convective mixing carries down O_3 from the residual layer and photochemical production maximizes. The similarities to the surface layer suggest that O_3 surface deposition at MKN cannot be ruled out as a contributor to the observed bias.

4 Conclusions

Although the Mt. Kenya GAW station is situated in equatorial Africa it is largely unaffected by African biomass burning emissions that are most prominent in the western parts of the continent but insignificant in Kenya. The local environment of the Mt. Kenya site is in general free of anthropogenic emissions and makes atmospheric baseline measurements possible. On only 2 % of all times local wildfire emissions influence the measurements. These events can easily be detected and removed from data analysis and therefore do not disturb the baseline character of the station. At the high altitude site night-time (21:00–04:00 UTC) measurements were in general representative of FT conditions, while day-time measurements were influenced by the ABL throughout the whole year and under different synoptic conditions, rendering day-time measurements not appropriate for atmospheric baseline estimation. The measurements at Mt. Kenya were found to be representative of six different catchment areas at different times of the year: eastern Africa throughout the whole year (21%), continental northern hemispheric air originating over the Arabian Peninsula and Pakistan throughout the whole year (16%), northern hemispheric free tropospheric background from January to May (6%), northern hemispheric air originating over India and crossing the northern Indian Ocean from November to April (17%), continental southern hemispheric air originating

in south-eastern Africa from April to October (18%) and southern Indian Ocean maritime air from April to November (21%).

The average overall night-time CO mixing ratio at MKN was 94±16 ppb. The CO annual cycle with two maxima in February and August indicates the influence of the oscillating monsoon circulation. The winter/spring maximum was caused by advection of northern hemispheric air that is enriched in CO during the boreal winter. In contrast, the summer maximum was observed during advection of southern hemispheric air loaded with emissions from biomass burning in southern Africa. Peak CO concentrations in the southern African biomass burning regions occur later (August/September) than at MKN. However, direct northward transport ceases when concentrations are maximal in southern Africa. Inter-annual variability in summer time CO could mostly be explained by a combination of changes in transport patterns and biomass burning intensity. The average overall night-time O_3 mixing ratio at MKN was 29±3 ppb. The annual cycle of O_3 was less pronounced than the one of CO. Mixing ratios were highest during the southern hemisphere biomass burning season from July to September and reached a minimum during the southward passage of the ITCZ during November.

The measurements at MKN are representative of air masses with little photochemical activity as indicated by weak O_3-CO correlations. The strongest correlations were found in air masses originating from the remote southern Indian Ocean, indicative of photochemical destruction. On the one hand, these weak O_3-CO correlations and the infrequent number of pollution events prove the baseline character of the station, on the other hand, the station is sometimes influenced by biomass burning events and can therefore be used as a platform to study aged biomass burning plumes. Biomass burning plumes observed at the site were between 3 to 5 days old, showed a strong O_3-CO correlation with slopes increasing from 0.2 after 3 days to 0.6 after 5 days.

Areal comparison of trajectory statistics using the MKN CO measurements with satellite-retrieved CO showed similar general patterns, but relative differences of −40 to +20%. The inter-comparison of the MKN O_3 measurements with O_3 soundings in Nairobi showed general agreement of the annual cycle, but also revealed a negative

offset of the MKN measurements when compared to the sounding observations at station altitude. This might indicate that O_3 deposition might influence the measurements at MKN even during night-time when compared to free tropospheric conditions.

The MKN GAW station is a very promising site for future studies of atmospheric chemistry in the equatorial western Indian Ocean and eastern Africa. The location of the site within the strong monsoonal currents crossing the Equator along the eastern edge of the African continent would allow for studies of inter-hemispheric exchange. The expansion of the ongoing measurement program will promote our understanding of the atmospheric chemistry over the remote Indian Ocean and eastern Africa. Future trend analysis will show the influence of increasing Asian emission on the marine environment of the Indian Ocean.

Acknowledgements. We gratefully acknowledge the financial support of MeteoSwiss. The establishment of the Mt. Kenya GAW station was supported by the World Bank through their Global Environmental Facility. We thank the authorities of the Mount Kenya National Park for their cooperation and the local technicians and workers for their work under often difficult conditions.

References

Aghedo, A. M., Schultz, M. G., and Rast, S.: The influence of African air pollution on regional and global tropospheric ozone, Atmos. Chem. Phys., 7, 1193–1212, 2007, http://www.atmos-chem-phys.net/7/1193/2007/. 17772

Andreae, M. O. and Merlet, P.: Emission of trace gases and aerosols from biomass burning, Global Biogeochem. Cy., 15, 955–966, 2001. 17771

Andreae, M. O., Anderson, B. E., Blake, D. R., Bradshaw, J. D., Collins, J. E., Gregory, G. L., Sachse, G. W., and Shipham, M. C.: Influence of Plumes from Biomass Burning on Atmospheric Chemistry over the Equatorial and Tropical South-Atlantic during Cite-3, J. Geophys. Res.-Atmos., 99, 12 793–12 808, 1994. 17792

Asnani, G.: Tropical Meteorology, Volume 1, Noble Printers, 603 pp., Pune, India, 1993. 17782

Brankov, E., Rao, S. T., and Porter, P. S.: A trajectory-clustering-correlation methodology for examining the long-range transport of air pollutants, Atmos. Environ., 32, 1525–1534, 1998. 17777

Bremer, H., Kar, J., Drummond, J. R., Nichitu, F., Zou, J. S., Liu, J., Gille, J. C., Deeter, M. N., Francis, G., Ziskin, D., and Warner, J.: Spatial and temporal variation of MOPITT CO in Africa and South America: A comparison with SHADOZ ozone and MODIS aerosol, J. Geophys. Res.-Atmos., 109, D12304, doi:10.1029/2003JD004234, 2004. 17782, 17792

Chameides, W. and Walker, J. C. G.: Photochemical Theory of Tropospheric Ozone, J. Geophys. Res., 78, 8751–8760, 1973. 17771

Chatfield, R. B. and Delany, A. C.: Convection Links Biomass Burning to Increased Tropical Ozone - However, Models Will Tend to Overpredict O3, J. Geophys. Res.-Atmos., 95, 18 473–18 488, 1990. 17772

Crutzen, P. J.: Photochemical reaction initiated by and influencing ozone in unpolluted tropospheric air, Tellus, 26, 45–55, 1974. 17771

Crutzen, P. J. and Andreae, M. O.: Biomass Burning in the Tropics – Impact on Atmospheric Chemistry and Biogeochemical Cycles, Science, 250, 1669–1678, 1990. 17771

de Gouw, J. A., Warneke, C., Scheeren, H. A., van der Veen, C., Bolder, M., Scheele, M. P., Williams, J., Wong, S., Lange, L., Fischer, H., and Lelieveld, J.: Overview of the trace gas measurements on board the Citation aircraft during the intensive field phase of INDOEX, J. Geophys. Res.-Atmos., 106, 28 453–28 467, 2001. 17785

de Laat, A. T. J., Lelieveld, J., Roelofs, G. J., Dickerson, R. R., and Lobert, J. M.: Source analysis of carbon monoxide pollution during INDOEX 1999, J. Geophys. Res.-Atmos., 106, 28 481–28 495, 2001. 17785

Deeter, M. N., Emmons, L. K., Francis, G. L., Edwards, D. P., Gille, J. C., Warner, J. X., Khattatov, B., Ziskin, D., Lamarque, J. F., Ho, S. P., Yudin, V., Attie, J. L., Packman, D., Chen, J., Mao, D., and Drummond, J. R.: Operational carbon monoxide retrieval algorithm and selected results for the MOPITT instrument, J. Geophys. Res.-Atmos., 108, 4399, doi:10.1029/202JD003186, 2003. 17794

Dorling, S. R., Davies, T. D., and Pierce, C. E.: Cluster-Analysis – a Technique for Estimating the Synoptic Meteorological Controls on Air and Precipitation Chemistry - Method and Applications, Atmos. Environ. A-Gen., 26, 2575–2581, 1992a. 17777

Dorling, S. R., Davies, T. D., and Pierce, C. E.: Cluster-Analysis – a Technique for Estimating the Synoptic Meteorological Controls on Air and Precipitation Chemistry – Results from Eskdalemuir, South Scotland, Atmos. Environ. A-Gen., 26, 2583–2602, 1992b. 17777

Edwards, D. P., Emmons, L. K., Gille, J. C., Chu, A., Atti, J.-L., Giglio, L., Wood, S. W., Haywood, J., Deeter, M. N., Massie, S. T., Ziskin, D., and Drummond, J. R.: Satellite-observed pollution

from Southern Hemisphere biomass burning, J. Geophys. Res., 111, D14312, doi:10.1029/2005JD006655, 2006a. 17782, 17787, 17794

Edwards, D. P., Petron, G., Novelli, P. C., Emmons, L. K., Gille, J. C., and Drummond, J. R.: Southern Hemisphere carbon monoxide interannual variability observed by Terra/Measurement of Pollution in the Troposphere (MOPITT), J. Geophys. Res.-Atmos., 111, D16303, doi:10.1029/2006JD007079, 2006b. 17773, 17789, 17790, 17794

Emmons, L. K., Deeter, M. N., Gille, J. C., Edwards, D. P., Attie, J. L., Warner, J., Ziskin, D., Francis, G., Khattatov, B., Yudin, V., Lamarque, J. F., Ho, S. P., Mao, D., Chen, J. S., Drummond, J., Novelli, P., Sachse, G., Coffey, M. T., Hannigan, J. W., Gerbig, C., Kawakami, S., Kondo, Y., Takegawa, N., Schlager, H., Baehr, J., and Ziereis, H.: Validation of Measurements of Pollution in the Troposphere (MOPITT) CO retrievals with aircraft in situ profiles, J. Geophys. Res.-Atmos., 109, D03309, doi:10.1029/2003JD004101, 2004. 17794

Findlater, J.: A Major Low-Level Air Current near Indian Ocean during Northern Summer, Q. J. Roy. Meteor. Soc., 95, 362–380, 1969. 17783

Fishman, J. and Seiler, W.: Correlative Nature of Ozone and Carbon-Monoxide in the Troposphere – Implications for the Tropospheric Ozone Budget, J. Geophys. Res.-Oc. Atm., 88, 3662–3670, 1983. 17771, 17778

Fishman, J., Solomon, S., and Crutzen, P. J.: Observational and Theoretical Evidence in Support of a Significant Insitu Photo-Chemical Source of Tropospheric Ozone, Tellus, 31, 432–446, 1979. 17771

Fishman, J., Hoell, J. M., Bendura, R. D., McNeil, R. J., and Kirchhoff, V. W. J. H.: NASA GTE TRACE A experiment (September October 1992): Overview, J. Geophys. Res.-Atmos., 101, 23 865–23 879, 1996. 17772

Garstang, M., Tyson, P. D., Swap, R., Edwards, M., Kallberg, P., and Lindesay, J. A.: Horizontal and vertical transport of air over southern Africa, J. Geophys. Res.-Atmos., 101, 23 721–23 736, 1996. 17786

Gatebe, C., Tyson, P., Annegarn, H., Piketh, S., and Helas, G.: A seasonal air transport climatology for Kenya, J. Geophys. Res.-Atmos., 104, 14 237–14 244, 1999. 17784

Giglio, L., Csiszar, I., and Justice, C. O.: Global distribution and seasonality of active fires as observed with the Terra and Aqua Moderate Resolution Imaging Spectroradiometer (MODIS) sensors, J. Geophys. Res., 111, G02016, doi:10.1029/2005JG000142, 2006. 17787

Goddard, L. and Graham, N. E.: Importance of the Indian Ocean for simulating rainfall anomalies over eastern and southern Africa, J. Geophys. Res.-Atmos., 104, 19 099–19 116, 1999.

17787
Harris, J. M. and Kahl, J. D.: A Descriptive Atmospheric Transport Climatology for the Mauna-Loa-Observatory, Using Clustered Trajectories, J. Geophys. Res.-Atmos., 95, 13 651–13 667, 1990. 17777
Hely, C., Dowty, P. R., Alleaume, S., Caylor, K. K., Korontzi, S., Swap, R. J., Shugart, H. H., and Justice, C. O.: Regional fuel load for two climatically contrasting years in southern Africa, J. Geophys. Res.-Atmos., 108, 8475, doi:10.1029/2002JD002341, 2003. 17787
Indeje, M., Semazzi, F. H. M., and Ogallo, L. J.: ENSO signals in East African rainfall seasons, Int. J. Climatol., 20, 19–46, 2000. 17787
IPCC: Climate Change 2001: The Scientific Basis. Contribution of Working Group I to the Third Assessment Report of the Intergovernmental Panel on Climate Change, Cambridge University Press, Cambridge, UK and New York, USA, 2001. 17771
ISO: 11222:2002 Air quality - Determination of the uncertainty of the time average of air quality measurements, Tech. Rep. 11222:2002, International Organization for Standardization (ISO), 2002. 17775
Jost, C., Trentmann, J., Sprung, D., Andreae, M. O., McQuaid, J. B., and Barjat, H.: Trace gas chemistry in a young biomass burning plume over Namibia: Observations and model simulations, J. Geophys. Res.-Atmos., 108, 8482, doi:10.1029/2002JD002431, 2003. 17792
Justice, C. O., Giglio, L., Korontzi, S., Owens, J., Morisette, J. T., Roy, D., Descloitres, J., Alleaume, S., Petitcolin, F., and Kaufman, Y.: The MODIS fire products, Remote Sens. Environ., 83, 244–262, 2002. 17787
Kaufman, L. and Rousseeuw, P.: Finding Groups in Data. An Introduction to Cluster Analysis, John Wiley and Sons, New York, 1990. 17777, 17778
Klausen, J., Zellweger, C., Buchmann, B., and Hofer, P.: Uncertainty and bias of surface ozone measurements at selected Global Atmosphere Watch sites, J. Geophys. Res.-Atmos., 108, 4622, doi:10.1029/2003JD003710, 2003. 17776
Klausen, J., Henne, S., Zellweger, C., and Buchmann, B.: System and Performance Audit for Surface Ozone an Carbon Monoxide at the Global GAW Station Mt. Kenya, Tech. Rep., Empa-WCC, 2006. 17776
Klonecki, A. and Levy, H.: Tropospheric chemical ozone tendencies in CO-CH4-NOy-H2O system: Their sensitivity to variations in environmental parameters and their application to a global chemistry transport model study, J. Geophys. Res.-Atmos., 102, 21 221–21 237, 1997. 17780

Lelieveld, J. and Dentener, F. J.: What controls tropospheric ozone?, J. Geophys. Res.-Atmos., 105, 3531–3551, 2000. 17772

Lelieveld, J., Crutzen, P. J., Ramanathan, V., Andreae, M. O., Brenninkmeijer, C. A. M., Campos, T., Cass, G. R., Dickerson, R. R., Fischer, H., de Gouw, J. A., Hansel, A., Jefferson, A., Kley, D., de Laat, A. T. J., Lal, S., Lawrence, M. G., Lobert, J. M., Mayol-Bracero, O. L., Mitra, A. P., Novakov, T., Oltmans, S. J., Prather, K. A., Reiner, T., Rodhe, H., Scheeren, H. A., Sikka, D., and Williams, J.: The Indian Ocean Experiment: Widespread air pollution from South and Southeast Asia, Science, 291, 1031–1036, 2001. 17772, 17782

Leroux, M.: The meteorology and climate of tropical Africa, Springer, London, 2001. 17782

Levy, H.: Normal Atmosphere – Large Radical and Formaldehyde Concentrations Predicted, Science, 173, 141–143, 1971. 17771

Lindesay, J. A., Andreae, M. O., Goldammer, J. G., Harris, G., Annegarn, H. J., Garstang, M., Scholes, R. J., and vanWilgen, B. W.: International Geosphere-Biosphere Programme International Global Atmospheric Chemistry SAFARI-92 field experiment: Background and overview, J. Geophys. Res.-Atmos., 101, 23 521–23 530, 1996. 17772

Loader, C.: Local regression and likelihood, Springer, New York, 1999. 17775

Logan, J. A., Prather, M. J., Wofsy, S. C., and Mcelroy, M. B.: Tropospheric Chemistry - a Global Perspective, J. Geophys. Res.-Oc. Atm., 86, 7210–7254, 1981. 17772

Marenco, A., Thouret, V., Ndlec, P., Smit, H., Helten, M., Kley, D., Karcher, F., Simon, P., Law, K., Pyle, J., Poschmann, G., Von Wrede, R., Hume, C., and Cook, T.: Measurement of ozone and water vapor by Airbus in-service aircraft: The MOZAIC airborne program, An overview, J. Geophys. Res.-Atmos., 103, 25 631–25 642, 1998. 17773

Martin, R. V., Jacob, D. J., Logan, J. A., Bey, I., Yantosca, R. M., Staudt, A. C., Li, Q. B., Fiore, A. M., Duncan, B. N., Liu, H. Y., Ginoux, P., and Thouret, V.: Interpretation of TOMS observations of tropical tropospheric ozone with a global model and in situ observations, J. Geophys. Res.-Atmos., 107, 4351, doi:10.1029/2001JD001480, 2002. 17773

Marufu, L., Dentener, F., Lelieveld, J., Andreae, M. O., and Helas, G.: Photochemistry of the African troposphere: Influence of biomass-burning emissions, J. Geophys. Res.-Atmos., 105, 14 513–14 530, 2000. 17772

Mauzerall, D. L., Logan, J. A., Jacob, D. J., Anderson, B. E., Blake, D. R., Bradshaw, J. D., Heikes, B., Sachse, G. W., Singh, H., and Talbot, B.: Photochemistry in biomass burning plumes and implications for tropospheric ozone over the tropical South Atlantic, J. Geophys. Res.-Atmos., 103, 8401–8423, 1998. 17792, 17795

Moody, J. L. and Galloway, J. N.: Quatifying the relationship between atmospheric transport and the chemical composition of precipitation on Bermuda, Tellus, 40B, 463–479, 1988. 17777
Nédélec, P., Cammas, J. P., Thouret, V., Athier, G., Cousin, J. M., Legrand, C., Abonnel, C., Lecoeur, F., Cayez, G., and Marizy, C.: An improved infrared carbon monoxide analyser for routine measurements aboard commercial Airbus aircraft: technical validation and first scientific results of the MOZAIC III programme, Atmos. Chem. Phys., 3, 1551–1564, 2003, http://www.atmos-chem-phys.net/3/1551/2003/. 17775
Newchurch, M. J., Liu, X., Kim, J. H., and Bhartia, P. K.: On the accuracy of Total Ozone Mapping Spectrometer retrievals over tropical cloudy regions, J. Geophys. Res.-Atmos., 106, 32 315–32 326, 2001. 17773
Novelli, P., Masarie, K., and Lang, P.: Distribution and recent changes of carbon monoxide in the lower troposhere, J. Geophys. Res.-Atmos., 103, 19 015–19 033, 1998a. 17775, 17782
Novelli, P. C., Connors, V. S., Reichle, H. G., Anderson, B. E., Brenninkmeijer, C. A. M., Brunke, E. G., Doddridge, B. G., Kirchhoff, V. W. J. H., Lam, K. S., Masarie, K. A., Matsuo, T., Parrish, D. D., Scheel, H. E., and Steele, L. P.: An internally consistent set of globally distributed atmospheric carbon monoxide mixing ratios developed using results from an intercomparison of measurements, J. Geophys. Res.-Atmos., 103, 19 285–19 293, 1998b. 17775
Novelli, P. C., Masarie, K. A., Lang, P. M., Hall, B. D., Myers, R. C., and Elkins, J. W.: Reanalysis of tropospheric CO trends: Effects of the 1997–1998 wildfires, J. Geophys. Res.-Atmos., 108, 4464, doi:10.1029/2002JD003031, 2003. 17773, 17775, 17782
Parrish, D. D., Holloway, J. S., Trainer, M., Murphy, P. C., Forbes, G. L., and Fehsenfeld, F. C.: Export of North American Ozone Pollution to the North Atlantic Ocean, Science, 259, 1436–1439, 1993. 17771, 17778
Parrish, D. D., Trainer, M., Holloway, J. S., Yee, J. E., Warshawsky, M. S., Fehsenfeld, F. C., Forbes, G. L., and Moody, J. L.: Relationships between ozone and carbon monoxide at surface sites in the North Atlantic region, J. Geophys. Res.-Atmos., 103, 13 357–13 376, 1998. 17778, 17790
Pickering, K. E., Thompson, A. M., Tao, W. K., Rood, R. B., McNamara, D. P., and Molod, A. M.: Vertical Transport by Convective Clouds – Comparisons of 3 Modeling Approaches, Geophys. Res. Lett., 22, 1089–1092, 1995. 17772
Press, W. H., Teukolsky, S. A., Vetterling, W. T., and Flannery, B. P.: Numerical Recipes in C, The Art of Scientific Computing, Cambridge University Press, Cambridge, UK, 2nd edn., 1992. 17778

R Development Core Team: R 2.2.1: A language and environment for statistical computing, R Foundation for Statistical Computing, http://www.R-project.org, 2005. 17778

Redelsperger, J. L., Thorncroft, C. D., Diedhiou, A., Lebel, T., Parker, D. J., and Polcher, J.: African monsoon multidisciplinary analysis - An international research project and field campaign, B. Am. Meteorol. Soc., 87, doi:10.1175/BAMS-87-12-1739, 2006. 17773

Reimann, S., Schaub, D., Stemmler, K., Folini, D., Hill, M., Hofer, P., Buchmann, B., Simmonds, P. G., Greally, B. R., and O'Doherty, S.: Halogenated greenhouse gases at the Swiss High Alpine Site of Jungfraujoch (3580 m asl): Continuous measurements and their use for regional European source allocation, J. Geophys. Res.-Atmos., 109, D05307, doi:10.1029/2003JD003923, 2004. 17793

Roberts, G., Wooster, M. J., Perry, G. L. W., Drake, N., Rebelo, L. M., and Dipotso, F.: Retrieval of biomass combustion rates and totals from fire radiative power observations: Application to southern Africa using geostationary SEVIRI imagery, J. Geophys. Res.-Atmos., 110, D21111, doi:10.1029/2005JD006018, 2005. 17788

Saraf, N., Beig, G., and Schultz, M.: Tropospheric distribution of ozone and its precursors over the tropical Indian Ocean, J. Geophys. Res.-Atmos., 108, 4636, doi:10.1029/2003JD003521, 2003. 17783

Sauvage, B., Thouret, V., Cammas, J. P., Gheusi, F., Athier, G., and Ndlec, P.: Tropospheric ozone over Equatorial Africa: regional aspects from the MOZAIC data, Atmos. Chem. Phys., 5, 311–335, 2005, http://www.atmos-chem-phys.net/5/311/2005/. 17773, 17786

Scholes, M. C., Matrai, P. A., Andreae, M. O., Smith, K. A., and Manning, M. R.: Biosphere-Atmosphere Interactions, in: Atomspheric Chemistry in a Changing World, edited by: Brasseur, G., Prinn, R. G., and Pszenny, A., 19–71 pp., Springer, Berlin, 2003. 17771

Seibert, P., Kromp-Kolb, H., Baltensperger, U., Jost, D. T., Schwikowski, M., Kasper, A., and Puxbaum, H.: Trajectory Analysis of Aerosol Measurements at High Alpine Sites, in: Transport and Transformation of Pollutants in the Troposphere, edited by: Borrell, P. M., Borrell, P., Cvitas, T., and Seiler, W., 689–693 pp., Academic Publishing, Den Haag, Netherlands, 1994. 17793

Silva, J. M. N., Pereira, J. M. C., Cabral, A. I., Sa, A. C. L., Vasconcelos, M. J. P., Mota, B., and Gregoire, J. M.: An estimate of the area burned in southern Africa during the 2000 dry season using SPOT-VEGETATION satellite data, J. Geophys. Res.-Atmos., 108, 8498, doi:10.1029/2002JD002320, 2003. 17787, 17788

Singh, H. B., Viezee, W., Chen, Y., Bradshaw, J., Sandholm, S., Blake, D., Blake, N., Heikes, B., Snow, J., Talbot, R., Browell, E., Gregory, G., Sachse, G., and Vay, S.: Biomass burning influences on the composition of the remote South Pacific troposphere: analysis based on observations from PEM-Tropics-A, Atmos. Environ., 34, 635–644, 2000. 17792

Singleton, A. T. and Reason, C. J. C.: Variability in the characteristics of cut-off low pressure systems over subtropical southern Africa, Int. J. Climatol., 27, 295–310, 2007. 17787

Slingo, J., Spencer, H., Hoskins, B., Berrisford, P., and Black, E.: The meteorology of the Western Indian Ocean, and the influence of the east African highlands, Philos. T. Roy. Soc. A, 363, 25–42, 2005. 17782

Stehr, J. W., Ball, W. P., Dickerson, R. R., Doddridge, B. G., Piety, C. A., and Johnson, J. E.: Latitudinal gradients in O-3 and CO during INDOEX 1999, J. Geophys. Res.-Atmos., 107, 8015, doi:10.1029/2001JD000446, 2002. 17785

Stohl, A.: Trajectory Statistics - A New Method to Establish Source-Receptor Relationships of Air Pollutants and its Application to the Transport of Particulate Sulfate in Europe, Atmos. Environ., 30, 579–587, 1996. 17793

Stohl, A.: Computation, accuracy and applications of trajectories – A review and bibliography, Atmos. Environ., 32, 947–966, 1998. 17777

Stohl, A. and Seibert, P.: Accuracy of trajectories as determined from the conservation of meteorological tracers, Q. J. Roy. Meteor. Soc., 124, 1465–1484, 1998. 17776

Stohl, A., Wotawa, G., Seibert, P., and Kromp-Kolb, H.: Interpolation Errors in Wind Fields as a Function of Spatial and Temporal Resolution and Their Impact on Different Types of Kinematic Trajectories, J. Appl. Meteorol., 34, 2149–2165, 1995. 17776

Swap, R. J., Annegarn, H. J., Suttles, J. T., King, M. D., Platnick, S., Privette, J. L., and Scholes, R. J.: Africa burning: A thematic analysis of the Southern African Regional Science Initiative (SAFARI 2000), J. Geophys. Res.-Atmos., 108, 8465, doi:10.1029/2003JD003747, 2003. 17772, 17787

Takegawa, N., Kondo, Y., Ko, M., Koike, M., Kita, K., Blake, D. R., Hu, W., Scott, C., Kawakami, S., Miyazaki, Y., Russell-Smith, J., and Ogawa, T.: Photochemical production of O-3 in biomass burning plumes in the boundary layer over northern Australia, Geophys. Res. Lett., 30, 1500, doi:10.1029/2003GL017017, 2003. 17792

Thompson, A. M.: The Oxidizing Capacity of the Earths Atmosphere – Probable Past and Future Changes, Science, 256, 1157–1165, 1992. 17772

Thompson, A. M., Witte, J. C., Freiman, M. T., Phahlane, N. A., and Coetzee, G. J. R.: Lusaka,

Zambia, during SAFARI-2000: Convergence of local and imported ozone pollution, Geophys. Res. Lett., 29, 1976, doi:10.1029/2002GL015399, 2002. 17786
Thompson, A. M., Witte, J. C., Oltmans, S. J., and Schmidlin, F. J.: Shadoz – A tropical ozonesonde-radiosonde network for the atmospheric community, B. Am. Meteorol. Soc., 85, 1549–1564, 2004. 17773, 17780, 17795
Ward, J. H.: Hierarchical Grouping to Optimize an Objective Function, J. Am. Stat. Assoc., 58, 236–244, 1963. 17777
Watson, C. E., Fishman, J., and Reichle, H. G.: The Significance of Biomass Burning as a Source of Carbon-Monoxide and Ozone in the Southern-Hemisphere Tropics – a Satellite Analysis, J. Geophys. Res.-Atmos., 95, 16 443–16 450, 1990. 17773
Webster, P. J., Moore, A. M., Loschnigg, J. P., and Leben, R. R.: Coupled ocean-atmosphere dynamics in the Indian Ocean during 1997–98, Nature, 401, 356–360, 1999. 17787
Wooster, M. J., Roberts, G., Perry, G. L. W., and Kaufman, Y. J.: Retrieval of biomass combustion rates and totals from fire radiative power observations: FRP derivation and calibration relationships between biomass consumption and fire radiative energy release, J. Geophys. Res.-Atmos., 110, D24311, doi:10.1029/2005JD006318, 2005. 17788
World Meteorological Organization: Global Atmosphere Watch (2008–2015), Strategic Plan, Tech. Rep., World Meteorological Organization, 2007. 17774
Yokelson, R. J., Bertschi, I. T., Christian, T. J., Hobbs, P. V., Ward, D. E., and Hao, W. M.: Trace gas measurements in nascent, aged, and cloud-processed smoke from African savanna fires by airborne Fourier transform infrared spectroscopy (AFTIR), J. Geophys. Res.-Atmos., 108, 8478, doi:10.1029/2002JD002322, 2003. 17787, 17792
Zellweger, C., Buchmann, B., Klausen, J., and Hofer, P.: System and Performance Audit for Surface Ozone, Global GAW Station Mt. Kenya, Tech. Rep., Empa-WCC, 2002. 17776
Zellweger, C., Klausen, J., and Buchmann, B.: System and Performance Audit for Surface Ozone an Carbon Monoxide at the Global GAW Station Mt. Kenya, Tech. rep., Empa-WCC, 2005. 17776
Zhang, L., Jacob, D. J., Bowman, K. W., Logan, J. A., Turquety, S., Hudman, R. C., Li, Q. B., Beer, R., Worden, H. M., Worden, J. R., Rinsland, C. P., Kulawik, S. S., Lampel, M. C., Shephard, M. W., Fisher, B. M., Eldering, A., and Avery, M. A.: Ozone-CO correlations determined by the TES satellite instrument in continental outflow regions, Geophys. Res. Lett., 33, L18804, doi:10.1029/2006GL026399, 2006. 17790

Table 1. Annual cycle of night-time (21:00–04:00 UTC) CO and O_3 mixing ratios (ppb) measured at MKN in the period 1 June 2002 to 1 June 2006. $\bar{x}$: Mean, u_x: expanded uncertainty (p<0.05) of the mean, α_{10}: 10% percentile, α_{90}: 90% percentile.

Month	CO				O_3			
	$\bar{x}$	u_x	α_{10}	α_{90}	$\bar{x}$	u_x	α_{10}	α_{90}
Jan	96	1.0	78	113	30	0.7	20	42
Feb	104	1.6	85	121	31	0.9	15	45
March	95	1.2	74	135	32	0.4	22	42
April	74	0.8	61	91	30	0.4	20	39
May	75	1.0	60	88	33	0.6	22	44
June	84	1.2	68	99	36	0.6	26	45
July	94	1.5	75	111	35	0.5	27	44
Aug	95	1.7	75	128	33	0.6	25	40
Sep	86	0.8	70	107	35	0.4	24	46
Oct	90	0.9	72	111	28	0.6	15	40
Nov	85	0.9	71	96	23	0.4	14	31
Dec	89	1.1	77	104	26	0.9	16	39

Table 2. Annual cycle of night-time CO and O_3 mixing ratios (ppb) for different air mass origins. Values given in parentheses are expanded uncertainties (p<0.05) of the mean.

Month	CO						O_3					
	EA	AP	AA	SIO	NA	NIO	EA	AP	AA	SIO	NA	NIO
Jan	86 (1)	98 (3)	95 (2)	97 (4)	– (–)	101 (1)	26 (1)	32 (1)	35 (1)	25 (2)	– (–)	30 (1)
Feb	103 (2)	110 (2)	103 (2)	77 (5)	– (–)	102 (3)	21 (2)	34 (1)	41 (2)	– (–)	– (–)	30 (1)
March	87 (2)	113 (4)	99 (4)	76 (2)	84 (7)	87 (1)	30 (1)	34 (1)	31 (1)	30 (3)	33 (5)	32 (1)
April	75 (1)	84 (3)	81 (6)	67 (1)	73 (1)	72 (1)	31 (1)	33 (3)	37 (6)	28 (1)	26 (1)	31 (1)
May	76 (1)	82 (2)	87 (1)	66 (1)	74 (1)	– (–)	34 (1)	39 (1)	41 (1)	26 (1)	31 (1)	– (–)
June	86 (3)	85 (2)	86 (3)	79 (3)	84 (1)	76 (4)	39 (1)	38 (1)	42 (2)	33 (1)	34 (1)	39 (2)
July	92 (3)	89 (3)	87 (7)	87 (3)	99 (2)	– (–)	35 (1)	36 (1)	43 (6)	33 (1)	35 (1)	– (–)
Aug	96 (4)	85 (2)	– (–)	87 (2)	109 (3)	84 (4)	32 (1)	35 (2)	– (–)	32 (1)	33 (1)	30 (1)
Sep	83 (2)	84 (2)	– (–)	86 (1)	91 (2)	85 (3)	35 (1)	37 (1)	– (–)	34 (1)	36 (1)	34 (2)
Oct	86 (1)	82 (2)	– (–)	91 (1)	97 (2)	82 (4)	27 (1)	20 (2)	– (–)	28 (1)	32 (1)	24 (3)
Nov	81 (1)	88 (1)	93 (3)	83 (2)	84 (4)	86 (1)	24 (1)	24 (1)	25 (3)	24 (1)	24 (3)	21 (1)
Dec	87 (2)	92 (2)	93 (6)	74 (8)	– (–)	89 (1)	27 (2)	29 (1)	36 (4)	20 (2)	– (–)	22 (1)

ACPD
7, 17769–17824, 2007

EGU

Table 3. Characteristics of detected biomass burning plumes. Values given in parenthesis are expanded uncertainties ($p<0.05$). CO and O_3 mixing ratios and fire counts are mean values.

Start	End	No.	R^2	Slope (ppb/ppb)	Age (d)	CO (ppb)	O_3 (ppb)	Fire Counts	Origin
3 February 2004	6 February 2004	22	0.86	0.22 (0.02)	3.1 (0.1)	179	45	1005	Sudan, Ethiopia
7 March 2004	10 March 2005	22	0.43	0.46 (0.15)	3.8 (0.2)	140	36	118	Sudan, Ethiopia
26 September 2004	30 September 2004	30	0.61	0.62 (0.12)	4.7 (0.3)	127	43	82	Mozambique, Madagascar
1 March 2006	5 March 2006	29	0.68	0.36 (0.05)	4.2 (0.1)	139	31	345	Sudan, Ethiopia

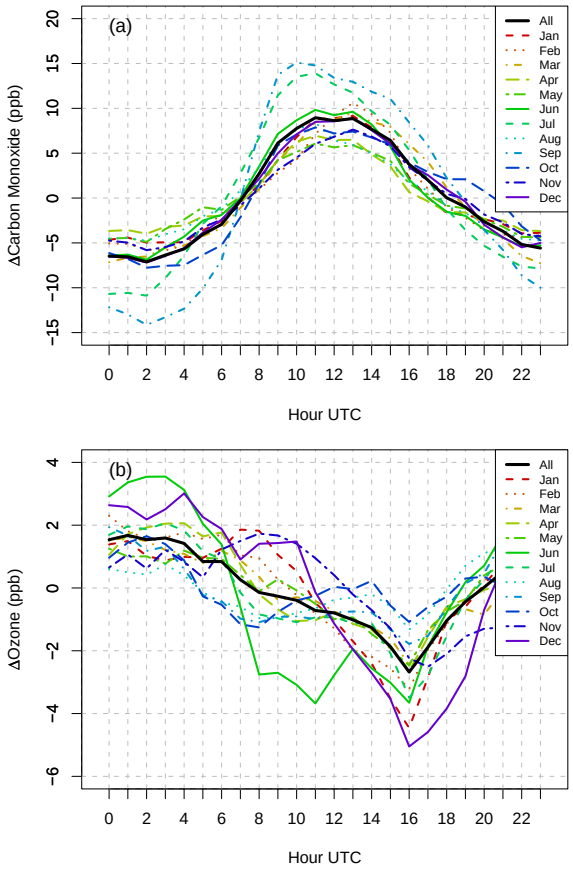

Fig. 1. Diurnal cycle of **(a)** carbon monoxide and **(b)** ozone. The black line represents the annual mean, while coloured lines refer to individual months. Note that the diurnal mean was subtracted before aggregation.

ACPD
7, 17769–17824, 2007

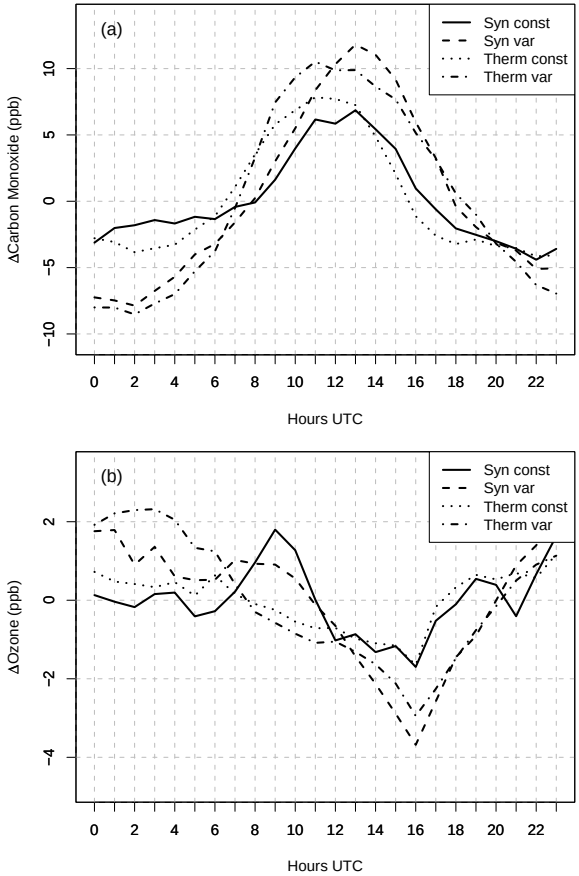

Fig. 2. Diurnal cycle of **(a)** carbon monoxide and **(b)** ozone anomalies for different categories (see text for details). There were 365 days (67%) within the therm/var category, 93 days (17%) in therm/const, 50 days (9%) in syn/var, and 40 days (7%) in syn/const. Note that the daily mean was subtracted before aggregation.

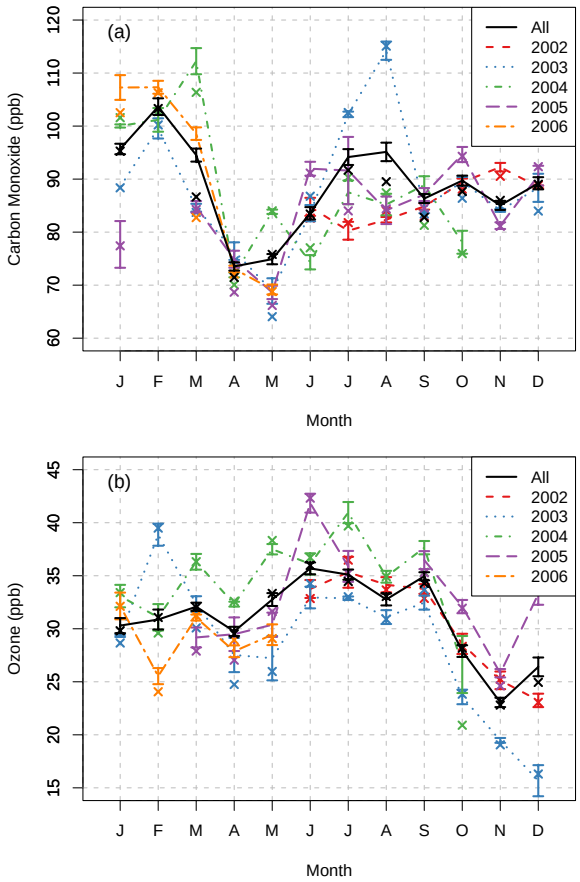

Fig. 3. Annual cycle of **(a)** carbon monoxide and **(b)** ozone. The black line represents the overall mean, while coloured lines refer to individual years. The error bars give the expanded uncertainty (95% confidence level) of the monthly mean, including uncertainty due to incomplete data coverage.

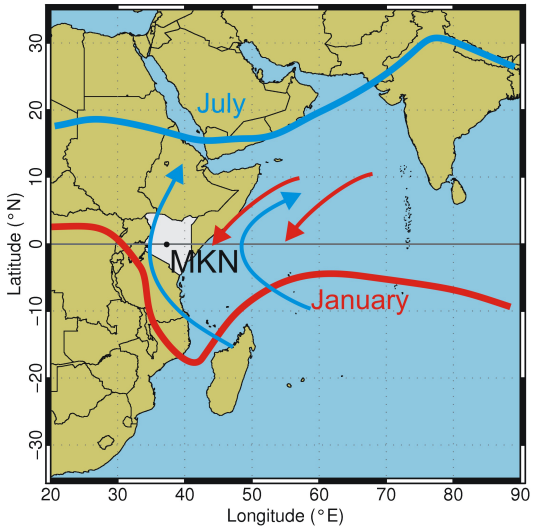

Fig. 4. Schematic position of the ITCZ (bold lines) and associated flow (arrows) over the western Indian Ocean for the month July and January. The position of the Mt. Kenya site is marked with a black dot.

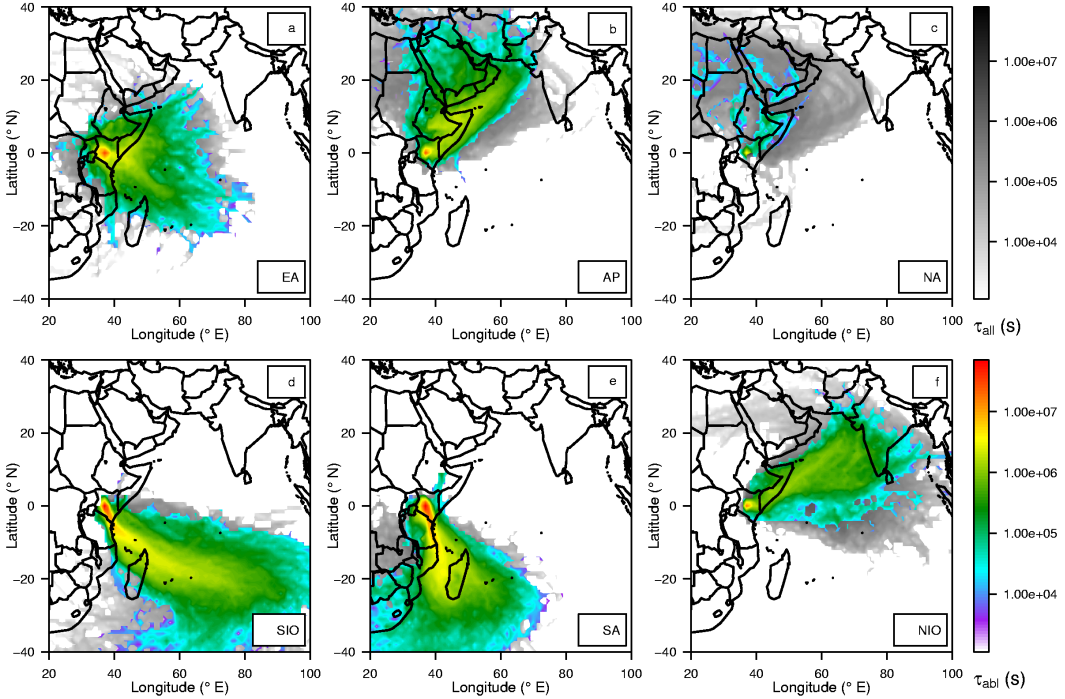

Fig. 5. Trajectory residence time composites for different trajectory clusters: (**a**, EA) East Africa, (**b**, AP) Arabian Peninsula, (**c**, NA) North Africa, (**d**, SIO) Southern Indian Ocean, (**e**, SA) Southern Africa, (**f**, NIO) Northern Indian Ocean. Residence times are given in seconds. The grey shades refer to residence times in the total tropospheric column, while the rainbow colours refer to residence times below 2000 m above model ground.

ACPD
7, 17769–17824, 2007

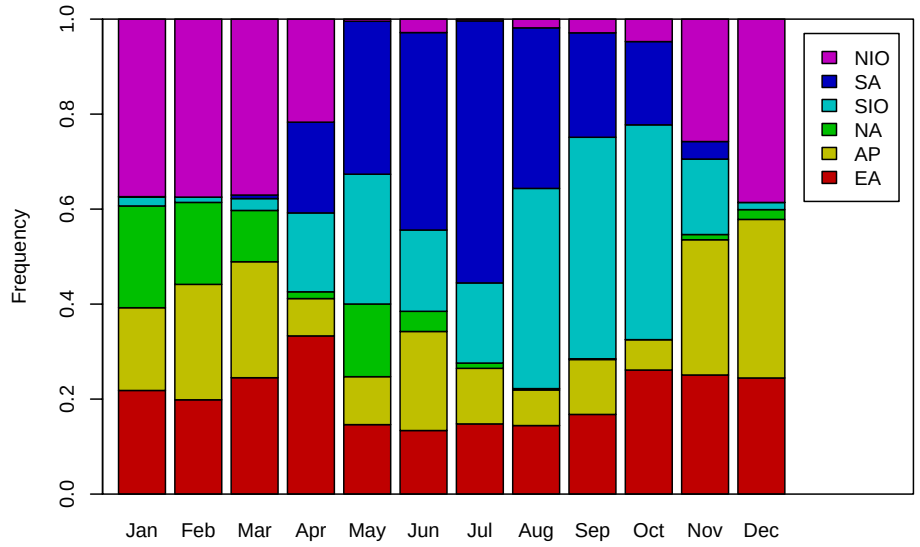

Fig. 6. Annual cycle of the relative frequency for different trajectory clusters.

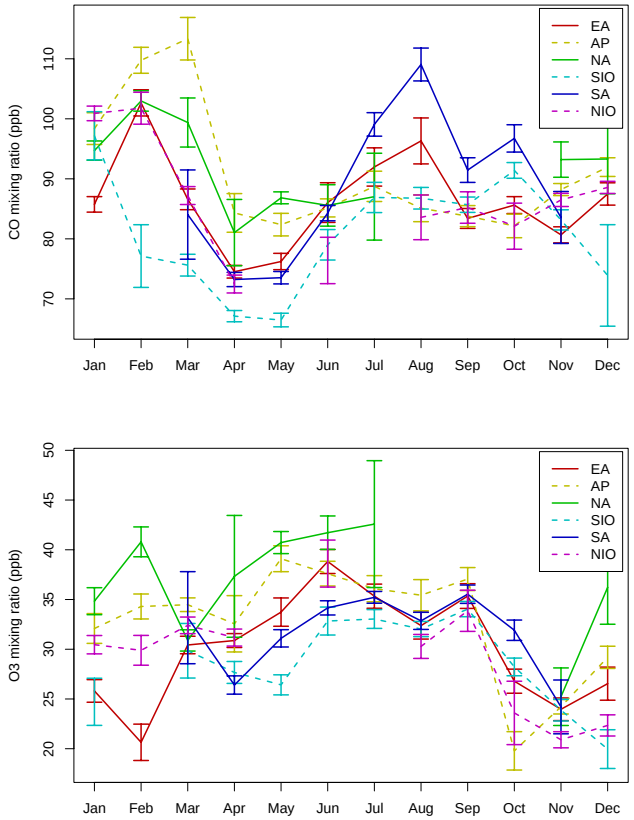

Fig. 7. Annual cycle of **(a)** carbon monoxide and **(b)** ozone for different trajectory clusters. The error bars give the expanded (k=2) uncertainty of the monthly cluster means.

ACPD
7, 17769–17824, 2007

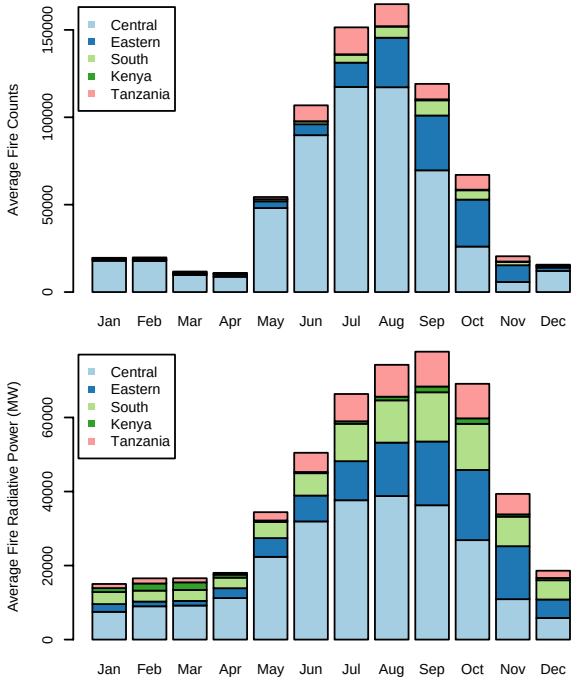

Fig. 8. Average annual cycle of fire counts (top) and fire radiative power (bottom) for different regions in southern and central Africa. Central: Zambia, Angola, Dem. Rep. Congo; eastern: Mozambique, Zimbabwe, Malawi, Madagascar; South: Botswana, South Africa, Swaziland, Namibia.

ACPD

7, 17769–17824, 2007

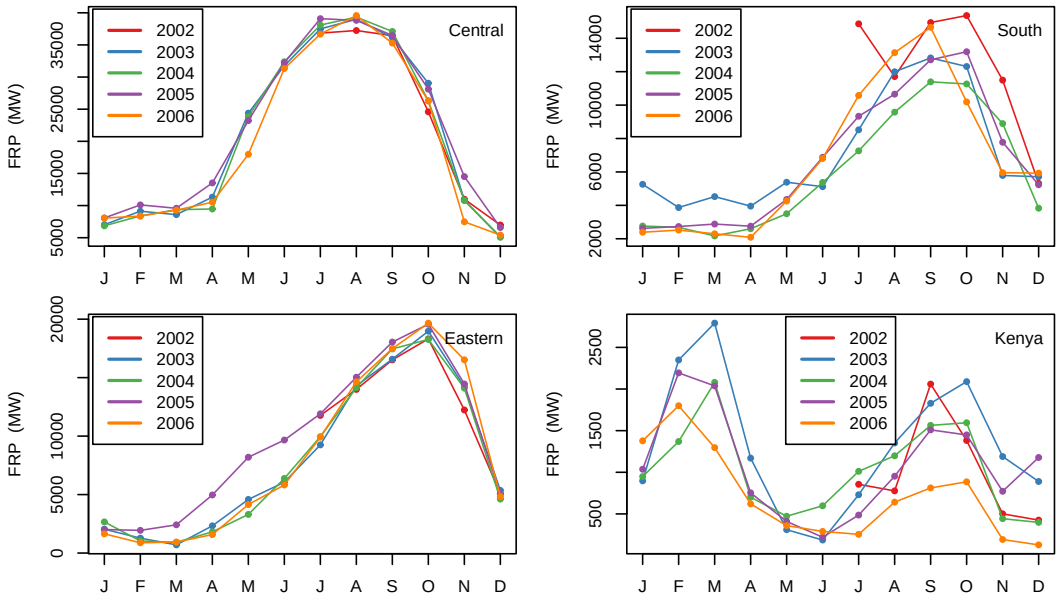

Fig. 9. Annual cycle of fire radiative power for different regions in southern and central Africa. See text for definition of regions. Note different y-scales.

ACPD
7, 17769–17824, 2007

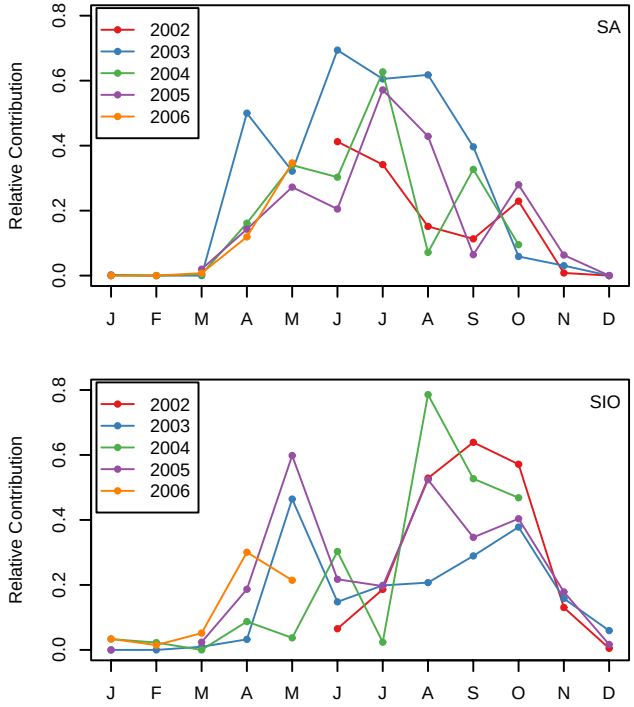

Fig. 10. Annual cycle of cluster contribution for different years for the South African cluster (SA, upper graph) and the Southern Indian Ocean cluster (SIO, lower graph).

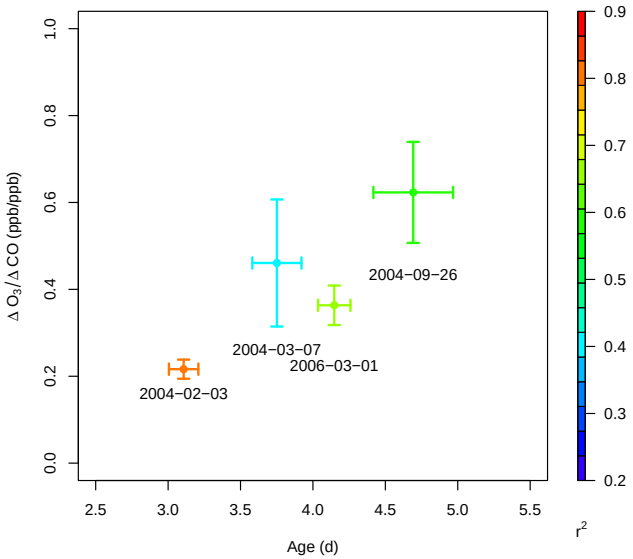

Fig. 11. O_3-CO regression slope versus plume age for detected biomass burning events. Error bars represent the uncertainty ($p<0.05$) of the slope and age, respectively. The given date marks the beginning of the pollution event.

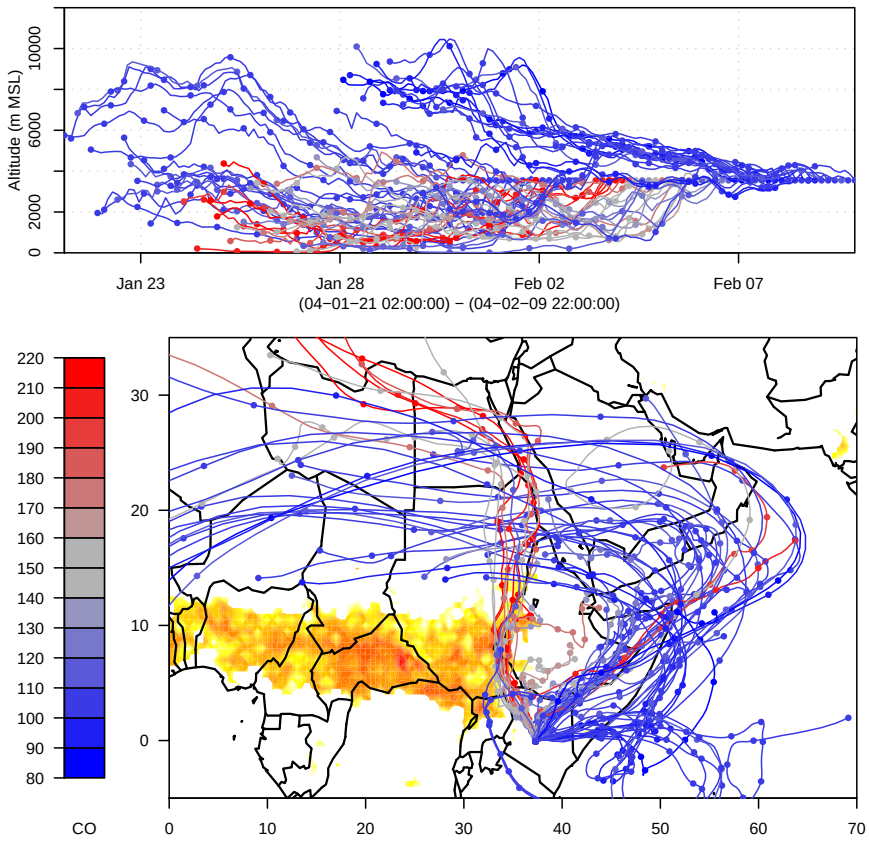

Fig. 12. Backward trajectories (colour refers to carbon monoxide concentration (ppb) measured at MKN) during a pollution event in February 2004. In addition, MODIS fire counts, totalled for the same period, are indicated in red shades for large and yellow shades for small fire count density. The map is left blank where no fires were detected.

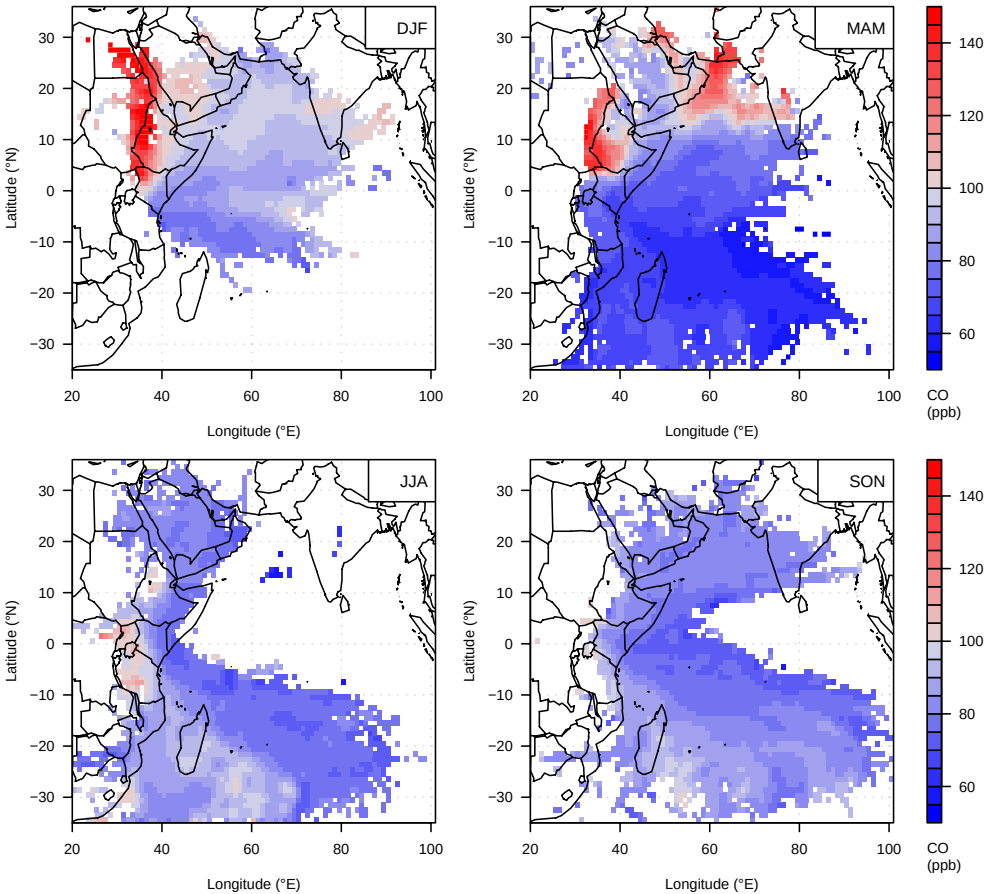

Fig. 13. Seasonal average CO distribution over the western Indian Ocean at 600 hPa as retrieved from trajectory statistics.

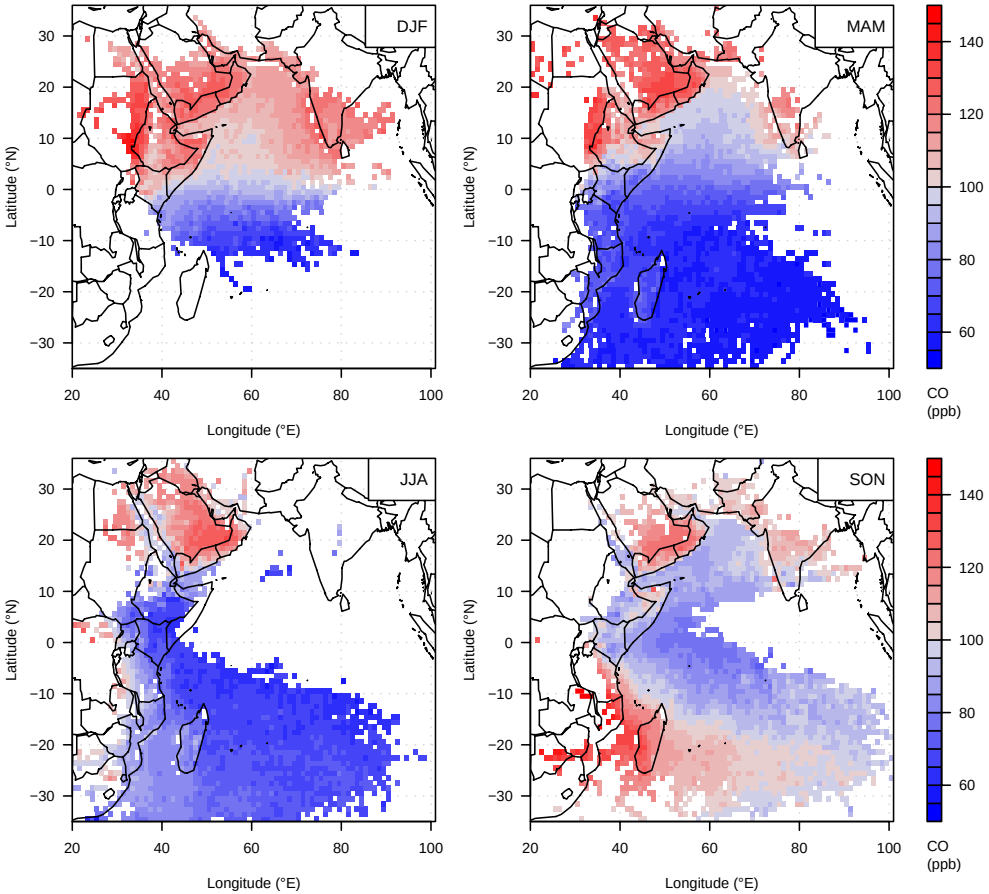

Fig. 14. Seasonal average CO distribution over the western Indian Ocean at 600 hPa as retrieved from night-time MOPITT scans. Grid cells that were not covered by the trajectory statistic are left blank.

ACPD
7, 17769–17824, 2007

EGU

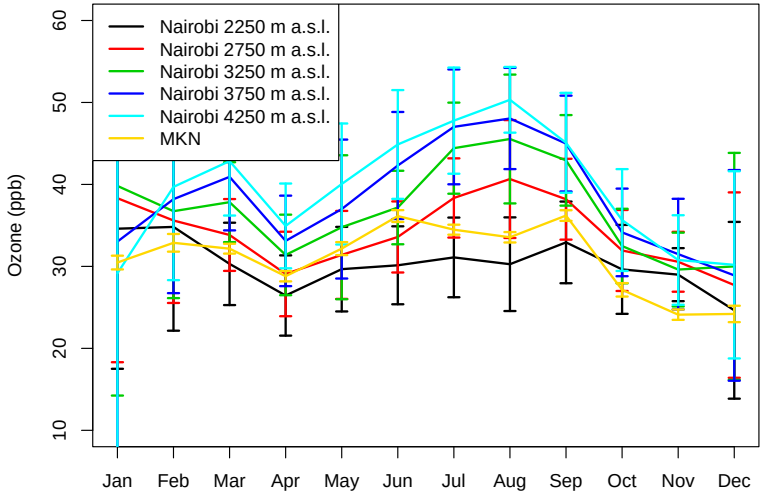

Fig. 15. Annual cycle of O_3 mixing ratios as measured at different altitude levels by Nairobi O_3 soundings and by MKN.